

Dynamic Mode Decomposition of High Reynolds Number Supersonic Jet Flows

Sami Yamouni*

Instituto Tecnológico de Aeronáutica, 12228-900 São José dos Campos, SP, Brazil

Carlos Junqueira-Junior[†], João Luiz F. Azevedo[‡]

Instituto de Aeronáutica e Espaço, 12228-903 São José dos Campos, SP, Brazil

William R. Wolf[§]

Universidade Estadual de Campinas, 13083-970 Campinas, SP, Brazil

Abstract

Current design constraints have encouraged the studies of aeroacoustic fields around compressible jet flows. The present work addresses the numerical study of unsteady turbulent jet flows as a preparation for future aeroacoustic analyses of main engine rocket plumes. An in-house large eddy simulation tool is used in order to reproduce high fidelity results of compressible jet flows. The large eddy simulation formulation is written using a second order numerical scheme for a finite difference spatial discretization. Numerical simulations of perfectly expanded jets are performed and the results are compared to the literature. Dynamic mode decompositions (DMD) of the jet flow, using large size three-dimensional snapshots, are performed. Three variables are analyzed, namely, the velocity magnitude, the vorticity magnitude and the divergence of velocity. In particular, two frequencies are identified and they are linked to flow structures observed in experiments performed by other authors in the literature. The spatial shapes of the corresponding dynamic modes are also discussed.

I. Introduction

One of the main design issues related to launch vehicles lies on noise emission originated by the complex interaction between the high-temperature/high-velocity exhaust gases and the atmospheric air. These emissions, which have high noise levels, can damage the launching structure or even be reflected upon the vehicle structure itself and the equipment onboard at the top of the vehicles. Moreover, the resulting pressure fluctuations can damage the solid structure of different parts of the launcher or the onboard scientific equipment by vibrational acoustic stress. Therefore, it is strongly recommended to consider the load resulted from acoustic sources over large launching vehicles during take-off and also during the transonic flight. Moreover, one cannot neglect the energy dissipation effect generated by the acoustic waves even if the vehicle is far from the ground. Theoretically, all chemical energy should be converted to kinetic energy. However, in reality, the noise generation consumes part of the chemical energy.

*Postdoctoral Research Fellow, Graduate Program on Computer Sciences and Electrical Engineering, Departamento de Ciência e Tecnologia Aeroespacial, DCTA/ITA; E-mail: sami.yamouni@gmail.com.

[†]Postdoctoral Research Fellow, Graduate Program on Computer Sciences and Electrical Engineering, Departamento de Ciência e Tecnologia Aeroespacial, DCTA/ITA; E-mail: junior.hmg@gmail.com.

[‡]Senior Research Engineer, Aerodynamics Division, Departamento de Ciência e Tecnologia Aeroespacial, DCTA/IAE/ALA; E-mail: joaoluiz.azevedo@gmail.com. Fellow AIAA.

[§]Assistant Professor, Faculty of Mechanical Engineering; E-mail: wolf@fem.unicamp.br. Member AIAA.

The acoustics design constraints have encouraged the studies of aeroacoustic fields around compressible jet flows. Instituto de Aeronautica e Espaço (IAE), in Brazil, is interested in this flow configuration for rocket design applications. Unsteady property fields of the flow are necessary for the aerocoustic study. Therefore, the present work addresses the numerical study of unsteady turbulent compressible jet flows as a preparatory step for such aeroacoustic applications in the future. Large eddy simulations (LES) are used in order to reproduce high fidelity results of the unsteady compressible jet flows.

One issue with the results of such large data sets resulting from LES calculations is precisely the large amount of data that has to be handled. Hence, with the objective of simplifying a complex flow into a low-dimensional representation containing the dominant dynamic structures, the use of different techniques has been proposed. Among these, Proper Orthogonal Decomposition (POD)¹⁻³ and Dynamic Mode Decomposition (DMD)⁴ are the more commonly used techniques in the fluid dynamics community. POD selects the modes depending on their energy content. However, this criterion is not necessarily the most appropriate, since the energy is not always the key parameter in order to identify the flow structures⁴ of interest. In contrast with POD, the modes computed from the DMD approach define characteristic frequencies of the flow. Hence, DMD is the chosen method for the intended application of the present work. It has already been applied to various flow configurations, such as cavity flows,^{4,5} shock wave-turbulent boundary layer interaction,⁶ boundary layer flows,^{7,8} cylinder flows,^{9,10} combustion chamber flows,^{11,12} wake behind a flexible membrane⁴ or jet flows.¹³⁻¹⁸ Several variations of the DMD algorithm have also been proposed. One can cite the optimal mode decomposition,¹⁹ the sparsity-promoting DMD,²⁰ the extended DMD,^{21,22} or the streaming DMD²³. Lately, an unbiased noise-robust method has been proposed by Hemati *et al.*²⁴ to overcome the adverse influence of measurement errors. This method can be combined with all the previously listed DMD algorithms.

Therefore, in this context, the main objective of the present work is to apply the DMD algorithm to the numerical data extracted from large eddy simulations of perfectly-expanded supersonic jet flows at $M = 1.4$. Due to the large dimension of this problem, the authors use the streaming version²³ of the *total-least squares* DMD formulation proposed by Hemati *et al.*²⁴ The DMD results are compared to numerical and experimental data available in the literature.

II. Navier-Stokes Equations

The numerical strategy used in the present study is based on the compressible Navier-Stokes equations formulated as

$$\frac{\partial \rho}{\partial t} + \frac{\partial}{\partial x_j} (\rho u_j) = 0, \quad (1)$$

$$\frac{\partial}{\partial t} (\rho u_i) + \frac{\partial}{\partial x_j} (\rho u_i u_j) + \frac{\partial p}{\partial x_i} - \frac{\partial \tau_{ij}}{\partial x_j} = 0, \quad (2)$$

$$\frac{\partial e}{\partial t} + \frac{\partial}{\partial x_j} [(e + p) u_j - \tau_{ij} u_i + q_j] = 0, \quad (3)$$

in which t and x_i are independent variables representing time and spatial coordinates of a Cartesian coordinate system \mathbf{x} , respectively. The components of the velocity vector \mathbf{u} are written as u_i , and $i = 1, 2, 3$. Density, pressure and total energy per mass unit are denoted by ρ , p and e , respectively. The heat flux vector, q_j , is given by

$$q_j = \kappa \frac{\partial T}{\partial x_j}, \quad (4)$$

where T is the static temperature and κ is the thermal conductivity coefficient, which can be expressed by

$$\kappa = \frac{\mu C_p}{Pr}. \quad (5)$$

The thermal conductivity coefficient is a function of the specific heat at constant pressure, C_p , of the Prandtl number, Pr , which is equal to 0.72 for air, and of the dynamic viscosity coefficient, μ . The latter can be calculated using Sutherland's law,

$$\mu(T) = \mu_\infty \left(\frac{T}{T_\infty} \right)^{\frac{3}{2}} \frac{T_0 + S_1}{T + S_1}, \quad \text{with } S_1 = 110.4 \text{ K}. \quad (6)$$

According to the Stokes hypothesis, the shear-stress tensor, τ_{ij} , for a Newtonian fluid can be written as

$$\tau_{ij} = 2\mu \left(S_{ij} - \frac{1}{3} \delta_{ij} S_{kk} \right), \quad (7)$$

in which the components of rate-of-strain tensor, S_{ij} , are given by

$$S_{ij} = \frac{1}{2} \left(\frac{\partial u_i}{\partial x_j} + \frac{\partial u_j}{\partial x_i} \right). \quad (8)$$

In order to close the system of equations the density, the static pressure and the static temperature are correlated by the equation of state given by

$$p = \rho RT, \quad (9)$$

where R is the gas constant, written as

$$R = C_p - C_v, \quad (10)$$

and C_v is the specif heat at constant volume. The total energy per mass unity is given by:

$$e = \frac{p}{\gamma - 1} + \frac{1}{2} \rho u_i u_i, \quad (11)$$

in which γ is the ratio of specific heats, written as $\gamma = C_p/C_v$.

III. Large Eddy Simulation Filtering

The large eddy simulation is based on the principle of scale separation, which is addressed as a filtering procedure in a mathematical formalism. A modified version of the the System I filtering approach²⁵ is used in present work. The original formulation neglects the double correlation term and it is written as

$$\begin{aligned} \frac{\partial \bar{p}}{\partial t} + \frac{\partial}{\partial x_j} (\bar{\rho} \tilde{u}_j) &= 0, \\ \frac{\partial}{\partial t} (\bar{\rho} \tilde{u}_i) + \frac{\partial}{\partial x_j} (\bar{\rho} \tilde{u}_i \tilde{u}_j) + \frac{\partial \bar{p}}{\partial x_i} - \frac{\partial \tilde{\tau}_{ij}}{\partial x_j} &= -\frac{\partial}{\partial x_j} [\sigma_{ij} - (\bar{\tau}_{ij} - \tilde{\tau}_{ij})], \\ \frac{\partial \tilde{e}}{\partial t} + \frac{\partial}{\partial x_j} [(\tilde{e} + \bar{p}) \tilde{u}_j] - \frac{\partial \tilde{\tau}_{ij} \tilde{u}_i}{\partial x_j} + \frac{\partial \tilde{q}_j}{\partial x_j} &= -B_1 - B_2 - B_3 + B_4 + B_5 + B_6 - B_7. \end{aligned} \quad (12)$$

The $(\tilde{\cdot})$ notation is used to represent a Frave averaged property. The SGS stress tensor components are written as σ_{ij} . The filtering procedure originates two new terms, $\tilde{\tau}_{ij}$ and \tilde{q}_j . These new terms are given by

$$\tilde{\tau}_{ij} = 2\mu \left(\tilde{S}_{ij} - \frac{1}{3} \delta_{ij} \tilde{S}_{kk} \right), \quad (13)$$

where

$$\tilde{S}_{ij} = \frac{1}{2} \left(\frac{\partial \tilde{u}_i}{\partial x_j} + \frac{\partial \tilde{u}_j}{\partial x_i} \right), \quad (14)$$

and

$$\tilde{q}_j = \tilde{\kappa} \frac{\partial \tilde{T}}{\partial x_j}, \quad (15)$$

in which

$$\tilde{\kappa} = \kappa \left(\tilde{T} \right) = \frac{\tilde{\mu} \left(\tilde{T} \right) C_p}{Pr}. \quad (16)$$

The SGS terms of the energy equation, B_i , are given by

$$B_1 = \frac{1}{(\gamma - 1)} \frac{\partial}{\partial x_j} (\overline{p u_j} - \bar{p} \tilde{u}_j) = \frac{\partial C_v Q_j}{\partial x_j}, \quad (17)$$

$$B_2 = \overline{p \frac{\partial u_k}{\partial x_k}} - \bar{p} \frac{\partial \tilde{u}_k}{\partial x_k} = \Pi_{dil}, \quad (18)$$

$$B_3 = \frac{\partial}{\partial x_j} (\sigma_{kj} \tilde{u}_k), \quad (19)$$

$$B_4 = \sigma_{kj} \frac{\partial}{\partial x_j} \tilde{u}_k, \quad (20)$$

$$B_5 = \overline{\tau_{kj} \frac{\partial}{\partial x_j} u_k} - \overline{\tau_{ij}} \frac{\partial}{\partial x_j} \tilde{u}_k = \epsilon, \quad (21)$$

$$B_6 = \frac{\partial}{\partial x_j} (\overline{\tau_{ij}} \tilde{u}_i - \check{\tau}_{ij} \tilde{u}_i) = \frac{\partial \mathcal{D}}{\partial x_j}, \quad (22)$$

$$B_7 = \frac{\partial}{\partial x_j} (\bar{q}_j - \check{q}_j). \quad (23)$$

The work of Vreman *et al.*²⁶ and Vreman²⁵ classify the influence of each term of System I and System II formulations on a 2-D temporal shear layer flow. The classification, including large, medium, small and negligible effects, is based on the L_2 norm of different terms of the filtered equations. One order of magnitude separates the norm of each class of terms. Garnier *et al.*²⁷ compile the analogy as presented in Tab. 1.

Table 1. Classification of System I terms

Large	convective \overline{NS}
Medium	diffusive \overline{NS} , B_1 , B_2 and B_3
Small	B_4 and B_5
Negligible	$\frac{\partial}{\partial x_j} (\overline{\tau_{ij}} - \check{\tau}_{ij})$, B_6 and B_7

In practice, the authors of the System I analogy neglect the non-linear terms occurring in the viscous terms and in the heat fluxes.²⁷ Moreover, some of the terms from the original System I set of equations, Eq. (12), such as B_4 and B_5 , cannot be written in conservative form. Only the terms with large and medium influence are considered in the present work. The SGS stress tensor components are written using the SGS viscosity,²⁸

$$\sigma_{ij} = -2\mu_{sgs} \left(\check{S}_{ij} - \frac{1}{3} \check{S}_{kk} \right) + \frac{1}{3} \delta_{ij} \sigma_{kk}. \quad (24)$$

The most important terms of the filtered energy equation are modeled based on the work of Eidson²⁹ and Vreman.²⁵ They are given by

$$B_1 + B_2 = -\frac{\partial}{\partial x_j} \left(\kappa_{sgs} \frac{\partial \tilde{T}}{\partial x_j} \right), \quad (25)$$

where

$$\kappa_{sgs} = \frac{\mu_{sgs} C_p}{Pr_{sgs}}. \quad (26)$$

Using Eqs. (24), (25), and (26), one can write a simplified version of the System I formulation as

$$\begin{aligned} \frac{\partial \bar{p}}{\partial t} + \frac{\partial}{\partial x_j} (\bar{p} \tilde{u}_j) &= 0, \\ \frac{\partial}{\partial t} (\bar{p} \tilde{u}_i) + \frac{\partial}{\partial x_j} (\bar{p} \tilde{u}_i \tilde{u}_j) + \frac{\partial \bar{p}}{\partial x_i} - \frac{\partial \tau_{ij}^{mod}}{\partial x_j} + \frac{1}{3} \frac{\partial}{\partial x_j} (\delta_{ij} \sigma_{ii}) &= 0, \\ \frac{\partial \check{\epsilon}}{\partial t} + \frac{\partial}{\partial x_j} [(\check{\epsilon} + \bar{p}) \tilde{u}_j] - \frac{\partial}{\partial x_j} (\tau_{ij}^{mod} \tilde{u}_i) + \frac{1}{3} \frac{\partial}{\partial x_j} [(\delta_{ij} \sigma_{ii}) \tilde{u}_i] + \frac{\partial q_j^{mod}}{\partial x_j} &= 0, \end{aligned} \quad (27)$$

where, τ_{ij}^{mod} and q_j^{mod} , include the viscous and the subgrid terms. They can be written as

$$\tau_{ij}^{mod} = 2(\mu + \mu_{sgs}) \left(S_{ij} - \frac{1}{3} \delta_{ij} S_{kk} \right) \quad (28)$$

and

$$q_j^{mod} = (\kappa + \kappa_{sgs}) \frac{\partial T}{\partial x_j}. \quad (29)$$

Previous work have shown that the subgrid scale terms are too small when compared to the truncation error of the second order numerical scheme used in the current research.³⁰⁻³² Therefore, an implicit LES is performed in which all subgrid scales terms, $[\cdot]_{sgs}$, introduced in Eqs. (28) and (29) are neglected.

IV. Transformation of Coordinates

The formulation used in the current work is written in the a general curvilinear coordinate system in order to facilitate the implementation and add more generality for the CFD tool. The modified System I set of equations, Eq. (27) can be written in a strong conservative form for a 3-D Cartesian coordinate system as

$$\frac{\partial \bar{Q}}{\partial t} + \frac{\partial \bar{E}}{\partial x} + \frac{\partial \bar{F}}{\partial y} + \frac{\partial \bar{G}}{\partial z} = 0, \quad (30)$$

where \bar{Q} stands for the filtered conservative properties vector given by

$$\bar{Q} = [\bar{\rho} \quad \bar{\rho} \tilde{u} \quad \bar{\rho} \tilde{v} \quad \bar{\rho} \tilde{w} \quad \check{e}]^T. \quad (31)$$

The flux vectors which represent both the inviscid and viscous fluxes, \bar{E} , \bar{F} and \bar{G} are written as

$$\bar{E} = \left\{ \begin{array}{c} \bar{\rho} \tilde{u} \\ \bar{\rho} \tilde{u}^2 + \bar{p} - \tau_{xx}^{mod} + \frac{1}{3} \sigma_{xx} \\ \bar{\rho} \tilde{u} \tilde{v} - \tau_{xy}^{mod} \\ \bar{\rho} \tilde{u} \tilde{w} - \tau_{xz}^{mod} \\ (\check{e} + \bar{p} - \tau_{xx}^{mod} + \frac{1}{3} \sigma_{xx}) \tilde{u} - \tau_{xy}^{mod} \tilde{v} - \tau_{xz}^{mod} \tilde{w} + q_x^{mod} \end{array} \right\}, \quad (32)$$

$$\bar{F} = \left\{ \begin{array}{c} \bar{\rho} \tilde{v} \\ \bar{\rho} \tilde{u} \tilde{v} - \tau_{xy}^{mod} \\ \bar{\rho} \tilde{v}^2 + \bar{p} - \tau_{yy}^{mod} + \frac{1}{3} \sigma_{yy} \\ \bar{\rho} \tilde{v} \tilde{w} - \tau_{yz}^{mod} \\ (\check{e} + \bar{p} - \tau_{yy}^{mod} + \frac{1}{3} \sigma_{yy}) \tilde{v} - \tau_{xy}^{mod} \tilde{u} - \tau_{yz}^{mod} \tilde{w} + q_y^{mod} \end{array} \right\}, \quad (33)$$

$$\bar{G} = \left\{ \begin{array}{c} \bar{\rho} \tilde{w} \\ \bar{\rho} \tilde{u} \tilde{w} - \tau_{xz}^{mod} \\ \bar{\rho} \tilde{v} \tilde{w} - \tau_{yz}^{mod} \\ \bar{\rho} \tilde{w}^2 + \bar{p} - \tau_{zz}^{mod} + \frac{1}{3} \sigma_{zz} \\ (\check{e} + \bar{p} - \tau_{zz}^{mod} + \frac{1}{3} \sigma_{zz}) \tilde{w} - \tau_{xz}^{mod} \tilde{u} - \tau_{yz}^{mod} \tilde{v} + q_z^{mod} \end{array} \right\}, \quad (34)$$

in which, u , v and w are the velocity components in the Cartesian coordinates, x , y and z respectively.

In the present work the chosen general coordinate transformation is given by

$$\begin{aligned} \mathcal{T} &= t, \\ \xi &= \xi(x, y, z, t), \\ \eta &= \eta(x, y, z, t), \\ \zeta &= \zeta(x, y, z, t). \end{aligned} \quad (35)$$

Throughout the present work, ξ is the axial jet flow direction, η is the radial direction and ζ is the azimuthal direction. The derivatives in the general curvilinear coordinate system are calculated as a function of the derivatives the Cartesian coordinate system by the chain rule. Therefore, one can write

$$\begin{pmatrix} \frac{\partial}{\partial \mathcal{T}} \\ \frac{\partial}{\partial \xi} \\ \frac{\partial}{\partial \eta} \\ \frac{\partial}{\partial \zeta} \end{pmatrix} = \begin{bmatrix} 1 & x_{\mathcal{T}} & y_{\mathcal{T}} & z_{\mathcal{T}} \\ 0 & x_{\xi} & y_{\xi} & z_{\xi} \\ 0 & x_{\eta} & y_{\eta} & z_{\eta} \\ 0 & x_{\zeta} & y_{\zeta} & z_{\zeta} \end{bmatrix} \begin{pmatrix} \frac{\partial}{\partial t} \\ \frac{\partial}{\partial x} \\ \frac{\partial}{\partial y} \\ \frac{\partial}{\partial z} \end{pmatrix}. \quad (36)$$

The Jacobian of the transformation, J , is calculated as the inverse of the determinant of the matrix in the chain rule presented in Eq. (36). Therefore, for the 3-D coordinate transformation, the Jacobian can be written as

$$J = (x_{\xi}y_{\eta}z_{\zeta} + x_{\eta}y_{\zeta}z_{\xi} + x_{\zeta}y_{\xi}z_{\eta} - x_{\xi}y_{\zeta}z_{\eta} - x_{\eta}y_{\xi}z_{\zeta} - x_{\zeta}y_{\eta}z_{\xi})^{-1}. \quad (37)$$

The metric terms are given by

$$\begin{aligned} \xi_x &= J(y_{\eta}z_{\zeta} - y_{\zeta}z_{\eta}), & \xi_y &= J(z_{\eta}x_{\zeta} - z_{\zeta}x_{\eta}), & \xi_z &= J(x_{\eta}y_{\zeta} - x_{\zeta}y_{\eta}), \\ \eta_x &= J(y_{\eta}z_{\xi} - y_{\xi}z_{\eta}), & \eta_y &= J(z_{\eta}x_{\xi} - z_{\xi}x_{\eta}), & \eta_z &= J(x_{\eta}y_{\xi} - x_{\xi}y_{\eta}), \\ \zeta_x &= J(y_{\xi}z_{\eta} - y_{\eta}z_{\xi}), & \zeta_y &= J(z_{\xi}x_{\eta} - z_{\eta}x_{\xi}), & \zeta_z &= J(x_{\xi}y_{\eta} - x_{\eta}y_{\xi}), \\ \xi_t &= -x_{\mathcal{T}}\xi_x - y_{\mathcal{T}}\xi_y - z_{\mathcal{T}}\xi_z, & \eta_t &= -x_{\mathcal{T}}\eta_x - y_{\mathcal{T}}\eta_y - z_{\mathcal{T}}\eta_z, & \zeta_t &= -x_{\mathcal{T}}\zeta_x - y_{\mathcal{T}}\zeta_y - z_{\mathcal{T}}\zeta_z. \end{aligned} \quad (38)$$

One can rewrite Eq. (30), in a conservative form, for the general curvilinear coordinate system as

$$\frac{\partial \hat{Q}}{\partial \mathcal{T}} + \frac{\partial \hat{E}}{\partial \xi} + \frac{\partial \hat{F}}{\partial \eta} + \frac{\partial \hat{G}}{\partial \zeta} = 0, \quad (39)$$

where

$$\hat{Q} = J^{-1}\bar{Q} = J^{-1}[\bar{\rho} \quad \bar{\rho}\tilde{u} \quad \bar{\rho}\tilde{v} \quad \bar{\rho}\tilde{w} \quad \bar{e}]^T, \quad (40)$$

and the new flux vectors are given by

$$\begin{aligned} \hat{E} &= J^{-1}(\xi_t\bar{Q} + \xi_x\bar{E} + \xi_y\bar{F} + \xi_z\bar{G}), \\ \hat{F} &= J^{-1}(\eta_t\bar{Q} + \eta_x\bar{E} + \eta_y\bar{F} + \eta_z\bar{G}), \\ \hat{G} &= J^{-1}(\zeta_t\bar{Q} + \zeta_x\bar{E} + \zeta_y\bar{F} + \zeta_z\bar{G}). \end{aligned} \quad (41)$$

Finally, the flux vectors are split in inviscid and viscous part in order to simplify the implementation. Therefore, Eq. (39) can be rewritten as

$$\frac{\partial \hat{Q}}{\partial \mathcal{T}} + \frac{\partial \hat{E}_e}{\partial \xi} + \frac{\partial \hat{F}_e}{\partial \eta} + \frac{\partial \hat{G}_e}{\partial \zeta} = \frac{\partial \hat{E}_v}{\partial \xi} + \frac{\partial \hat{F}_v}{\partial \eta} + \frac{\partial \hat{G}_v}{\partial \zeta}, \quad (42)$$

where the inviscid flux vectors, \hat{E}_e , \hat{F}_e and \hat{G}_e , are given by

$$\hat{E}_e = J^{-1} \begin{pmatrix} \bar{\rho}U \\ \bar{\rho}\tilde{u}U + \bar{p}\xi_x \\ \bar{\rho}\tilde{v}U + \bar{p}\xi_y \\ \bar{\rho}\tilde{w}U + \bar{p}\xi_z \\ (\check{e} + \bar{p})U - \bar{p}\xi_t \end{pmatrix}, \quad (43)$$

$$\hat{F}_e = J^{-1} \begin{pmatrix} \bar{\rho}V \\ \bar{\rho}\tilde{u}V + \bar{p}\eta_x \\ \bar{\rho}\tilde{v}V + \bar{p}\eta_y \\ \bar{\rho}\tilde{w}V + \bar{p}\eta_z \\ (\check{e} + \bar{p})V - \bar{p}\eta_t \end{pmatrix}, \quad (44)$$

$$\hat{G}_e = J^{-1} \begin{Bmatrix} \bar{\rho}W \\ \bar{\rho}\tilde{u}W + \bar{p}\zeta_x \\ \bar{\rho}\tilde{v}W + \bar{p}\zeta_y \\ \bar{\rho}\tilde{w}W + \bar{p}\zeta_z \\ (\check{\epsilon} + \bar{p})W - \bar{p}\zeta_t \end{Bmatrix}, \quad (45)$$

in which the contravariant velocity components, U , V and W , are calculated as

$$\begin{aligned} U &= \xi_t + \xi_x \bar{u} + \xi_y \bar{v} + \xi_z \bar{w}, \\ V &= \eta_t + \eta_x \bar{u} + \eta_y \bar{v} + \eta_z \bar{w}, \\ W &= \zeta_t + \zeta_x \bar{u} + \zeta_y \bar{v} + \zeta_z \bar{w}. \end{aligned} \quad (46)$$

The viscous flux vectors, \hat{E}_v , \hat{F}_v and \hat{G}_v , are written as

$$\hat{E}_v = J^{-1} \begin{Bmatrix} 0 \\ \xi_x (\tau_{xx}^{mod} - \frac{1}{3}\sigma_{xx}) + \xi_y \tau_{xy}^{mod} + \xi_z \tau_{xz}^{mod} \\ \xi_x \tau_{xy}^{mod} + \xi_y (\tau_{yy}^{mod} - \frac{1}{3}\sigma_{yy}) + \xi_z \tau_{yz}^{mod} \\ \xi_x \tau_{xz}^{mod} + \xi_y \tau_{yz}^{mod} + \xi_z (\tau_{zz}^{mod} - \frac{1}{3}\sigma_{zz}) \\ \xi_x \beta_x + \xi_y \beta_y + \xi_z \beta_z \end{Bmatrix}, \quad (47)$$

$$\hat{F}_v = J^{-1} \begin{Bmatrix} 0 \\ \eta_x (\tau_{xx}^{mod} - \frac{1}{3}\sigma_{xx}) + \eta_y \tau_{xy}^{mod} + \eta_z \tau_{xz}^{mod} \\ \eta_x \tau_{xy}^{mod} + \eta_y (\tau_{yy}^{mod} - \frac{1}{3}\sigma_{yy}) + \eta_z \tau_{yz}^{mod} \\ \eta_x \tau_{xz}^{mod} + \eta_y \tau_{yz}^{mod} + \eta_z (\tau_{zz}^{mod} - \frac{1}{3}\sigma_{zz}) \\ \eta_x \beta_x + \eta_y \beta_y + \eta_z \beta_z \end{Bmatrix}, \quad (48)$$

$$\hat{G}_v = J^{-1} \begin{Bmatrix} 0 \\ \zeta_x (\tau_{xx}^{mod} - \frac{1}{3}\sigma_{xx}) + \zeta_y \tau_{xy}^{mod} + \zeta_z \tau_{xz}^{mod} \\ \zeta_x \tau_{xy}^{mod} + \zeta_y (\tau_{yy}^{mod} - \frac{1}{3}\sigma_{yy}) + \zeta_z \tau_{yz}^{mod} \\ \zeta_x \tau_{xz}^{mod} + \zeta_y \tau_{yz}^{mod} + \zeta_z (\tau_{zz}^{mod} - \frac{1}{3}\sigma_{zz}) \\ \zeta_x \beta_x + \zeta_y \beta_y + \zeta_z \beta_z \end{Bmatrix}, \quad (49)$$

where β_x , β_y and β_z are defined as

$$\begin{aligned} \beta_x &= \left(\tau_{xx}^{mod} - \frac{1}{3}\sigma_{xx} \right) \tilde{u} + \tau_{xy}^{mod} \tilde{v} + \tau_{xz}^{mod} \tilde{w} - q_x^{mod}, \\ \beta_y &= \tau_{xy}^{mod} \tilde{u} + \left(\tau_{yy}^{mod} - \frac{1}{3}\sigma_{yy} \right) \tilde{v} + \tau_{yz}^{mod} \tilde{w} - q_y^{mod}, \\ \beta_z &= \tau_{xz}^{mod} \tilde{u} + \tau_{yz}^{mod} \tilde{v} + \left(\tau_{zz}^{mod} - \frac{1}{3}\sigma_{zz} \right) \tilde{w} - q_z^{mod}. \end{aligned} \quad (50)$$

V. Dimensionless LES Formulation

A convenient nondimensionalisation is necessary in order to achieve a consistent implementation of the governing equations of motion. Dimensionless formulation yields to a more general numerical tool. There is no need to change the formulation for each configuration intended to be simulated. Moreover, dimensionless formulation scales all the necessary properties to the same order of magnitude which is a computational advantage.³³ Dimensionless variables are presented in the present section in order perform the nondimensionalisation of Eq. (42).

The dimensionless time, $\underline{\mathcal{T}}$, is written as function of the freestream speed of sound and of a reference length, D ,

$$\underline{\mathcal{T}} = \mathcal{T} \frac{a_\infty}{l}. \quad (51)$$

In the current work, D represents the jet entrance diameter. This reference length is also applied to write the dimensionless length,

$$\underline{l} = \frac{l}{D}. \quad (52)$$

The dimensionless velocity components are obtained using the freestream speed of sound

$$\underline{vel} = \frac{v}{a_\infty} \quad vel = u, v, w. \quad (53)$$

Dimensionless pressure and energy are calculated as

$$\underline{p} = \frac{p}{\rho_\infty a_\infty^2}, \quad (54)$$

$$\underline{e} = \frac{e}{\rho_\infty a_\infty^2}. \quad (55)$$

Dimensionless density, $\underline{\rho}$, temperature, \underline{T} and viscosity, $\underline{\mu}$, are calculated using freestream properties

$$\underline{\rho} = \frac{\rho}{\rho_\infty}. \quad (56)$$

One can use the dimensionless properties described above in order to write the dimensionless form of the LES equations as

$$\frac{\partial \underline{\hat{Q}}}{\partial \underline{T}} + \frac{\partial \underline{\hat{E}}_e}{\partial \underline{\xi}} + \frac{\partial \underline{\hat{F}}_e}{\partial \underline{\eta}} + \frac{\partial \underline{\hat{G}}_e}{\partial \underline{\zeta}} = \frac{M_j}{Re} \left(\frac{\partial \underline{\hat{E}}_v}{\partial \underline{\xi}} + \frac{\partial \underline{\hat{F}}_v}{\partial \underline{\eta}} + \frac{\partial \underline{\hat{G}}_v}{\partial \underline{\zeta}} \right), \quad (57)$$

where the underlined terms are calculated using non dimensional properties. The jet Mach and Reynolds numbers are based on the mean jet inlet velocity, U_j , the freestream speed of sound, a_∞ , density, ρ_∞ , viscosity, μ_∞ and the reference length, D ,

$$M_j = \frac{U_j}{a_\infty}, \quad Re = \frac{\rho_\infty U_j D}{\mu_\infty}. \quad (58)$$

VI. Numerical Formulation

The governing equations previously described are discretized in a structured finite difference context for general curvilinear coordinate system.³³ The numerical flux is calculated through a central difference scheme with the explicit addition of the anisotropic artificial dissipation of Turkel and Vatsa.³⁴ The time integration is performed by an explicit, 2nd-order, 5-stage Runge-Kutta scheme.^{35,36} Conserved properties and artificial dissipation terms are properly treated near boundaries in order to assure the physical correctness of the numerical formulation.

VI.A. Spatial Discretization

For the sake of simplicity, the formulation discussed in the present section is no longer written using bars, underbars, etc. However, the reader should notice that the equations are dimensionless and filtered. The LES equations, presented in Eq. (57), are discretized in space in a finite difference fashion and, then, rewritten as

$$\left(\frac{\partial Q}{\partial T} \right)_{i,j,k} = -RHS_{i,j,k}, \quad (59)$$

where RHS is the right hand side of the equation and it is written as function of the numerical flux vectors at the interfaces between grid points,

$$\begin{aligned} RHS_{i,j,k} = & \frac{1}{\Delta \xi} \left(\mathbf{E}_{e(i+\frac{1}{2},j,k)} - \mathbf{E}_{e(i-\frac{1}{2},j,k)} - \mathbf{E}_{v(i+\frac{1}{2},j,k)} + \mathbf{E}_{v(i-\frac{1}{2},j,k)} \right) \\ & \frac{1}{\Delta \eta} \left(\mathbf{F}_{e(i,j+\frac{1}{2},k)} - \mathbf{F}_{e(i,j-\frac{1}{2},k)} - \mathbf{F}_{v(i,j+\frac{1}{2},k)} + \mathbf{F}_{v(i,j-\frac{1}{2},k)} \right) \\ & \frac{1}{\Delta \zeta} \left(\mathbf{G}_{e(i,j,k+\frac{1}{2})} - \mathbf{G}_{e(i,j,k-\frac{1}{2})} - \mathbf{G}_{v(i,j,k+\frac{1}{2})} + \mathbf{G}_{v(i,j,k-\frac{1}{2})} \right). \end{aligned} \quad (60)$$

For the general curvilinear coordinate case $\Delta\xi = \Delta\eta = \Delta\zeta = 1$. The anisotropic artificial dissipation method of Turkel and Vatsa³⁴ is implemented through the modification of the inviscid flux vectors, \mathbf{E}_e , \mathbf{F}_e and \mathbf{G}_e . The numerical scheme is nonlinear and allows the selection between artificial dissipation terms of second and fourth differences, which is very important for capturing discontinuities in the flow. The numerical fluxes are calculated at interfaces in order to reduce the size of the calculation cell and, therefore, facilitate the implementation of second derivatives since the the concept of numerical fluxes vectors is used for flux differencing. Only internal interfaces receive the corresponding artificial dissipation terms, and differences of the viscous flux vectors use two neighboring points of the interface.

The inviscid flux vectors, with the addition of the artificial dissipation contribution, can be written as

$$\begin{aligned}\mathbf{E}_{e(i\pm\frac{1}{2},j,k)} &= \frac{1}{2} (\mathbf{E}_{e(i,j,k)} + \mathbf{E}_{e(i\pm 1,j,k)}) - J^{-1} \mathbf{d}_{(i\pm\frac{1}{2},j,k)}, \\ \mathbf{F}_{e(i,j,\pm\frac{1}{2},k)} &= \frac{1}{2} (\mathbf{F}_{e(i,j,k)} + \mathbf{F}_{e(i,j,\pm 1,k)}) - J^{-1} \mathbf{d}_{(i,j,\pm\frac{1}{2},k)}, \\ \mathbf{G}_{e(i,j,k\pm\frac{1}{2})} &= \frac{1}{2} (\mathbf{G}_{e(i,j,k)} + \mathbf{G}_{e(i,j,k\pm 1)}) - J^{-1} \mathbf{d}_{(i,j,k\pm\frac{1}{2})},\end{aligned}\quad (61)$$

in which the $\mathbf{d}_{(i\pm 1,j,k)}$, $\mathbf{d}_{(i,j,\pm 1,k)}$ and $\mathbf{d}_{(i,j,k\pm 1)}$ terms are the Turkel and Vatsa³⁴ artificial dissipation terms in the i , j , and k directions respectively. The scaling of the artificial dissipation operator in each coordinate direction is weighted by its own spectral radius of the corresponding flux Jacobian matrix, which gives the non-isotropic characteristics of the method.³³ The artificial dissipation contribution in the ξ direction is given by

$$\begin{aligned}\mathbf{d}_{(i+\frac{1}{2},j,k)} &= \lambda_{(i+\frac{1}{2},j,k)} \left[\epsilon_{(i+\frac{1}{2},j,k)}^{(2)} (\mathcal{W}_{(i+1,j,k)} - \mathcal{W}_{(i,j,k)}) \right. \\ &\quad \left. \epsilon_{(i+\frac{1}{2},j,k)}^{(4)} (\mathcal{W}_{(i+2,j,k)} - 3\mathcal{W}_{(i+1,j,k)} + 3\mathcal{W}_{(i,j,k)} - \mathcal{W}_{(i-1,j,k)}) \right],\end{aligned}\quad (62)$$

in which

$$\epsilon_{(i+\frac{1}{2},j,k)}^{(2)} = k^{(2)} \max \left(\nu_{(i+1,j,k)}^d, \nu_{(i,j,k)}^d \right), \quad (63)$$

$$\epsilon_{(i+\frac{1}{2},j,k)}^{(4)} = \max \left[0, k^{(4)} - \epsilon_{(i+\frac{1}{2},j,k)}^{(2)} \right]. \quad (64)$$

The original article³⁴ recommends using $k^{(2)} = 0.25$ and $k^{(4)} = 0.016$ for the dissipation artificial constants. The pressure gradient sensor, $\nu_{(i,j,k)}^d$, for the ξ direction is written as

$$\nu_{(i,j,k)}^d = \frac{|p_{(i+1,j,k)} - 2p_{(i,j,k)} + p_{(i-1,j,k)}|}{p_{(i+1,j,k)} - 2p_{(i,j,k)} + p_{(i-1,j,k)}}. \quad (65)$$

The \mathcal{W} vector from Eq. (62) is calculated as a function of the conserved variable vector, \hat{Q} , written in Eq. (40). The formulation intends to keep the total enthalpy constant in a final converged steady solution, which is the correct result for the Navier-Stokes equations with $Re \rightarrow \infty$. This approach is also valid for the viscous formulation because the dissipation terms are added to the inviscid flux terms, in which they are really necessary to avoid nonlinear instabilities of the numerical formulation. The \mathcal{W} vector is given by

$$\mathcal{W} = \hat{Q} + [0 \ 0 \ 0 \ 0 \ p]^T. \quad (66)$$

The spectral radius-based scaling factor, λ , for the i -th direction is written

$$\lambda_{(i+\frac{1}{2},j,k)} = \frac{1}{2} \left[(\overline{\lambda}_\xi)_{(i,j,k)} + (\overline{\lambda}_\xi)_{(i+1,j,k)} \right], \quad (67)$$

where

$$\overline{\lambda}_\xi_{(i,j,k)} = \lambda_\xi \left[1 + \left(\frac{\lambda_\eta}{\lambda_\xi} \right)^{0.5} + \left(\frac{\lambda_\zeta}{\lambda_\xi} \right)^{0.5} \right]. \quad (68)$$

The spectral radii, λ_ξ , λ_η and λ_ζ are given by

$$\begin{aligned}\lambda_\xi &= |U| + a\sqrt{\xi_x^2 + \eta_y^2 + \zeta_z^2}, \\ \lambda_\eta &= |V| + a\sqrt{\xi_x^2 + \eta_y^2 + \zeta_z^2}, \\ \lambda_\zeta &= |W| + a\sqrt{\xi_x^2 + \eta_y^2 + \zeta_z^2},\end{aligned}\quad (69)$$

in which, U , V and W are the contravariant velocity components in the ξ , η and ζ , previously written in Eq. (47), and a is the local speed of sound, which can be written as

$$a = \sqrt{\frac{\gamma p}{\rho}}. \quad (70)$$

The calculation of artificial dissipation terms for the other coordinate directions are completely similar and, therefore, they are not discussed in the present work.

VI.B. Time Marching Method

The time marching method used in the present work is a 2nd-order, 5-step Runge-Kutta scheme based on the work of Jameson and co-workers.^{35,36} The time integration can be written as

$$\begin{aligned} Q_{(i,jk)}^{(0)} &= Q_{(i,jk)}^{(n)}, \\ Q_{(i,jk)}^{(l)} &= Q_{(i,jk)}^{(0)} - \alpha_l \Delta t_{(i,jk)} RHS_{(i,jk)}^{(l-1)} \quad l = 1, 2 \dots 5, \\ Q_{(i,jk)}^{(n+1)} &= Q_{(i,jk)}^{(5)}, \end{aligned} \quad (71)$$

in which Δt is the time step and n and $n + 1$ indicate the property values at the current and at the next time step, respectively. The literature^{35,36} recommends

$$\alpha_1 = \frac{1}{4}, \quad \alpha_2 = \frac{1}{6}, \quad \alpha_3 = \frac{3}{8}, \quad \alpha_4 = \frac{1}{2}, \quad \alpha_5 = 1, \quad (72)$$

in order to improve the numerical stability of the time integration. The present scheme is theoretically stable for $CFL \leq 2\sqrt{2}$, under a linear analysis.³³

VII. Boundary Conditions

The present section presents all boundary conditions used for the turbulent compressible jet flow simulation such as inlet, outlet, centerline and far field boundary conditions. Moreover, the numerical treatment of the centerline singularity and the implementation of the periodic boundary in the azimuthal direction are also discussed in the end of the section.

VII.A. Far Field Boundary

Riemann invariants³⁷ are used to implement far field boundary conditions. They are derived from the characteristic relations for the Euler equations. At the interface of the outer boundary, the following expressions apply

$$\mathbf{R}^- = \mathbf{R}_\infty^- = q_{n_\infty} - \frac{2}{\gamma - 1} a_\infty, \quad (73)$$

$$\mathbf{R}^+ = \mathbf{R}_e^+ = q_{n_e} - \frac{2}{\gamma - 1} a_e, \quad (74)$$

where ∞ and e indexes stand for the property in the freestream and in the internal region, respectively. q_n is the velocity component normal to the outer surface, defined as

$$q_n = \mathbf{u} \cdot \vec{n}, \quad (75)$$

and \vec{n} is the unit outward normal vector

$$\vec{n} = \frac{1}{\sqrt{\eta_x^2 + \eta_y^2 + \eta_z^2}} [\eta_x \ \eta_y \ \eta_z]^T. \quad (76)$$

Equation (75) assumes that the η direction is pointing from the jet to the external boundary. Solving for q_n and a , one can obtain

$$q_{nf} = \frac{\mathbf{R}^+ + \mathbf{R}^-}{2}, \quad a_f = \frac{\gamma - 1}{4} (\mathbf{R}^+ - \mathbf{R}^-). \quad (77)$$

The index f is linked to the property at the boundary surface and will be used to update the solution at this boundary. For a subsonic exit boundary, $0 < q_{n_e}/a_e < 1$, the velocity components are derived from internal properties as

$$\begin{aligned} u_f &= u_e + (q_{nf} - q_{n_e})\eta_x, \\ v_f &= v_e + (q_{nf} - q_{n_e})\eta_y, \\ w_f &= w_e + (q_{nf} - q_{n_e})\eta_z. \end{aligned} \tag{78}$$

Density and pressure properties are obtained by extrapolating the entropy from the adjacent grid node,

$$\rho_f = \left(\frac{\rho_e^\gamma a_f^2}{\gamma p_e} \right)^{\frac{1}{\gamma-1}}, \quad p_f = \frac{\rho_f a_f^2}{\gamma}.$$

For a subsonic entrance, $-1 < q_{n_e}/a_e < 0$, properties are obtained similarly from the freestream variables as

$$\begin{aligned} u_f &= u_\infty + (q_{nf} - q_{n_\infty})\eta_x, \\ v_f &= v_\infty + (q_{nf} - q_{n_\infty})\eta_y, \\ w_f &= w_\infty + (q_{nf} - q_{n_\infty})\eta_z, \end{aligned} \tag{79}$$

$$\rho_f = \left(\frac{\rho_\infty^\gamma a_f^2}{\gamma p_\infty} \right)^{\frac{1}{\gamma-1}}. \tag{80}$$

For a supersonic exit boundary, $q_{n_e}/a_e > 1$, the properties are extrapolated from the interior of the domain as

$$\begin{aligned} \rho_f &= \rho_e, \\ u_f &= u_e, \\ v_f &= v_e, \\ w_f &= w_e, \\ e_f &= e_e, \end{aligned} \tag{81}$$

and for a supersonic entrance, $q_{n_e}/a_e < -1$, the properties are extrapolated from the freestream variables as

$$\begin{aligned} \rho_f &= \rho_\infty, \\ u_f &= u_\infty, \\ v_f &= v_\infty, \\ w_f &= w_\infty, \\ e_f &= e_\infty. \end{aligned} \tag{82}$$

VII.B. Entrance Boundary

For a jet-like configuration, the entrance boundary is divided in two areas: the jet and the area above it. The jet entrance boundary condition is implemented through the use of the 1-D characteristic relations for the 3-D Euler equations for a flat velocity profile. The set of properties then determined is computed from within and from outside the computational domain. For the subsonic entrance, the v and w components of the velocity are extrapolated by a zero-order extrapolation from inside the computational domain and the angle of flow entrance is assumed fixed. The rest of the properties are obtained as a function of the jet Mach number, which is a known variable.

$$\begin{aligned} (u)_{1,j,k} &= u_j, \\ (v)_{1,j,k} &= (v)_{2,j,k}, \\ (w)_{1,j,k} &= (w)_{2,j,k}. \end{aligned} \tag{83}$$

The dimensionless total temperature and total pressure are defined with the isentropic relations:

$$T_t = 1 + \frac{1}{2}(\gamma - 1)M_\infty^2 \quad \text{and} \quad P_t = \frac{1}{\gamma}(T_t)^{\gamma/(\gamma-1)}. \quad (84)$$

The dimensionless static temperature and pressure are deduced from Eq. (84), resulting in

$$(T)_{1,j,k} = \frac{T_t}{1 + \frac{1}{2}(\gamma - 1)(u^2 + v^2 + w^2)_{1,j,k}} \quad \text{and} \quad (p)_{1,j,k} = \frac{1}{\gamma}(T)_{1,j,k}^{\gamma/(\gamma-1)}. \quad (85)$$

For the supersonic case, all conserved variables receive jet property values.

The far field boundary conditions are implemented outside of the jet area in order to correctly propagate information coming from the inner domain of the flow to the outer region of the simulation. However, in the present case, ξ , instead of η , as presented in the previous subsection, is the normal direction used to define the Riemann invariants.

VII.C. Exit Boundary Condition

At the exit plane, the same reasoning of the jet entrance boundary is applied. This time, for a subsonic exit, the pressure is obtained from the outside and all other variables are extrapolated from the interior of the computational domain by a zero-order extrapolation. The conserved variables are obtained as

$$(\rho)_{I_{MAX},j,k} = \frac{(p)_{I_{MAX},j,k}}{(\gamma - 1)(e)_{I_{MAX}-1,j,k}}, \quad (86)$$

$$(\vec{u})_{I_{MAX},j,k} = (\vec{u})_{I_{MAX}-1,j,k}, \quad (87)$$

$$(e_i)_{I_{MAX},j,k} = (\rho)_{I_{MAX},j,k} \left[(e)_{I_{MAX}-1,j,k} + \frac{1}{2}(\vec{u})_{I_{MAX},j,k} \cdot (\vec{u})_{I_{MAX},j,k} \right], \quad (88)$$

in which I_{MAX} stands for the last point of the mesh in the axial direction. For the supersonic exit, all properties are extrapolated from the interior domain.

VII.D. Centerline Boundary Condition

The centerline boundary is a singularity of the coordinate transformation, and, hence, an adequate treatment of this boundary must be provided. The conserved properties are extrapolated from the adjacent longitudinal plane and are averaged in the azimuthal direction in order to define the updated properties at the centerline of the jet.

The fourth-difference terms of the artificial dissipation scheme, used in the present work, are carefully treated in order to avoid the five-point difference stencils at the centerline singularity. If one considers the flux balance at one grid point near the centerline boundary in a certain coordinate direction, let w_j denote a component of the \mathcal{W} vector from Eq. (66) and \mathbf{d}_j denote the corresponding artificial dissipation term at the mesh point j . In the present example, $(\Delta w)_{j+\frac{1}{2}}$ stands for the difference between the solution at the interface for the points $j+1$ and j . The fourth-difference of the dissipative fluxes from Eq. (62) can be written as

$$\mathbf{d}_{j+\frac{1}{2}} = (\Delta w)_{j+\frac{3}{2}} - 2(\Delta w)_{j+\frac{1}{2}} + (\Delta w)_{j-\frac{1}{2}}. \quad (89)$$

Considering the centerline and the point $j = 1$, as presented in Fig. 1, the calculation of $\mathbf{d}_{1+\frac{1}{2}}$ demands the $(\Delta w)_{\frac{1}{2}}$ term, which is unknown since it is outside the computation domain. In the present work a extrapolation is performed and given by

$$(\Delta w)_{\frac{1}{2}} = -(\Delta w)_{1+\frac{1}{2}}. \quad (90)$$

This extrapolation modifies the calculation of $\mathbf{d}_{1+\frac{1}{2}}$ that can be written as

$$\mathbf{d}_{j+\frac{1}{2}} = (\Delta w)_{j+\frac{3}{2}} - 3(\Delta w)_{j+\frac{1}{2}}. \quad (91)$$

The approach is plausible since the centerline region is smooth and it does not have high gradients of properties.

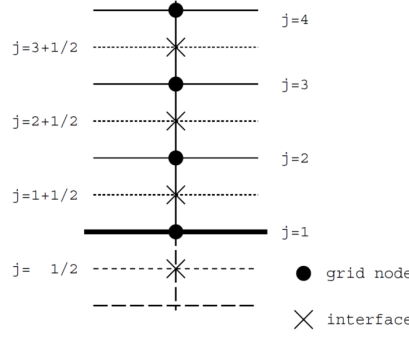


Figure 1. Boundary point distribution in the calculation of dissipation operator at the centerline.³³

VII.E. Periodic Boundary Condition

A periodic condition is implemented between the first ($K = 1$) and the last point in the azimuthal direction ($K = K_{MAX}$) in order to close the 3-D computational domain. There are no boundaries in this direction, since all the points are inside the domain. The first and the last points, in the azimuthal direction, are superposed in order to facilitate the boundary condition implementation which is given by

$$\begin{aligned}
 (\rho)_{i,j,K_{MAX}} &= (\rho)_{i,j,1}, \\
 (u)_{i,j,K_{MAX}} &= (u)_{i,j,1}, \\
 (v)_{i,j,K_{MAX}} &= (v)_{i,j,1}, \\
 (w)_{i,j,K_{MAX}} &= (w)_{i,j,1}, \\
 (e)_{i,j,K_{MAX}} &= (e)_{i,j,1}.
 \end{aligned} \tag{92}$$

VIII. Dynamic Mode Decomposition

VIII.A. Theoretical Framework

The DMD method provides a spatio-temporal decomposition of the flow into a set of dynamic modes that are derived from time-resolved snapshots. For example, a generic flow variable, $\mathbf{x}_{DMD}(x, y, z, t)$, where x, y, z and t stand for spatial coordinates and time, respectively, can be represented by

$$\mathbf{x}_{DMD}(x, y, z, t) = \sum_{i=1}^{m-1} a_i \exp(\lambda_i t) \phi_i(x, y, z). \tag{93}$$

Here, a_i and λ_i are the amplitude and the frequency of the spatial mode ϕ_i . The underlying mathematics is closely related to the idea of the Arnoldi algorithm.⁴ This flow variable, extracted from the simulation, can be represented in the form of a snapshot sequence $\mathbf{X} = [\mathbf{x}(t_1) \mathbf{x}(t_2) \cdots \mathbf{x}(t_m)] \in \mathbb{R}^{n \times m}$, where $\mathbf{x}(t_i) \in \mathbb{R}^n$ is the i -th snapshot, m denotes the number of snapshots and n , the spatial dimension of each time snapshot. Each snapshot, $\mathbf{x}(t_i)$, contains a set of variables depending on the user's choice. The present study is designed to collect data regularly separated in time by Δt even though recent techniques allow irregularly spaced sampling in time of the data.³⁸ The authors assume that there exists a linear operator $\mathcal{A} \in \mathbb{R}^{n \times n}$ connecting two consecutive snapshot giving

$$\mathbf{x}_{i+1} = \mathcal{A} \mathbf{x}_i \quad \text{for } i = 1, \dots, m-1. \tag{94}$$

The \mathcal{A} operator is an approximation of the Koopman operator,³⁹ whose eigen-elements can approximate the underlying dynamics of the flow, even if such dynamics is nonlinear. The objective of the DMD is the determination of these characteristics. The selection of the eigen-elements of \mathcal{A} is a matter of importance since the accuracy of the results, as well as the computational costs, both depend significantly on the method of choice. The strategy used in the present work is a combination of the total least-squares DMD, described

in Ref. 24, and the streaming DMD algorithm presented in Hemati *et al.*²³ The former technique provides a noise-aware DMD technique while the latter allows the assimilation “on-the-fly” of new incoming snapshots and it can even theoretically include an infinite number, m , of snapshots. Hemati *et al.*⁴⁰ ran successfully this combined technique to analyze the dynamics of the flow separation over a flat plate. In practice, the \mathcal{A} DMD operator of Eq. (94) can be defined as $\mathcal{A} = \mathbf{Y}\mathbf{X}^+$ using the previously defined snapshot matrix, \mathbf{X} , and its time-shifted version $\mathbf{Y} = [\mathbf{x}(t_1 + \Delta t) \ \mathbf{x}(t_2 + \Delta t) \ \cdots \ \mathbf{x}(t_m + \Delta t)]$. In this relation, \mathbf{X}^+ stands for the Moore-Penrose pseudoinverse of \mathbf{X} . The solution of the problem in the present form is prohibitively expensive in terms of CPU and memory costs. The streaming DMD approach suggests a solution to reformulate \mathcal{A} in order to be able to handle large dimension problems. First, the augmented snapshot matrix, $\mathbf{Z} = [\mathbf{X} \ \mathbf{Y}]^T$, is built.²⁴ After substitution, a low-dimensional version of \mathcal{A} , $\tilde{\mathcal{A}}$, can be obtained under the form

$$\tilde{\mathcal{A}} = \mathbf{Q}_x^T \begin{bmatrix} \mathbf{0} & \mathbf{I} \end{bmatrix} \mathbf{Q}_z \mathbf{G}_z \mathbf{Q}_z^T \begin{bmatrix} \mathbf{0} \\ \mathbf{I} \end{bmatrix} \mathbf{Q}_x \mathbf{G}_x^+ \in \mathbb{R}^{r \times r}, \quad (95)$$

where r is the rank of \mathbf{X} , \mathbf{Q}_x and \mathbf{Q}_z are obtained from the QR-decomposition of \mathbf{X} and \mathbf{Z} , respectively. Hence, one could write that $\mathbf{X} = \mathbf{Q}_x \mathbf{R}_x$ and $\mathbf{Z} = \mathbf{Q}_z \mathbf{R}_z$. Therefore, one can also write that $\mathbf{G}_z = \mathbf{R}_z \mathbf{R}_z^T$ and $\mathbf{G}_x = \mathbf{R}_x \mathbf{G}_z \mathbf{R}_z^T$. This procedure allows an incremental update of new available snapshots, without storing all of them in memory. Moreover, in this expression, the total number snapshot, m , does not appear anymore. During the streaming DMD process, a POD compression is included allowing the user to choose the rank of the DMD operator, r . The DMD modes and frequencies are given by the eigenvectors and eigenvalues of $\tilde{\mathcal{A}}$, such that ϕ_i is the i -th eigenvector with the associated eigenvalue, μ_i . Hence, the associated growth rate and frequency of the i -th DMD mode are given by

$$\sigma_i = \frac{\log(|\mu_i|)}{\Delta t} \quad \text{and} \quad \omega_i = \frac{\arg(\mu_i)}{\Delta t}. \quad (96)$$

Finally, $\lambda_i = \log(\mu_i)/\Delta t$. Another interesting aspect of the DMD, is that knowing the first snapshot and the eigenvalues of the DMD operator, one can predict the temporal behavior of the mode. Indeed, using a discretized version of Eq. (93) expressed at any time instant $k = 1, \dots, m-1$,

$$\mathbf{x}_k = \sum_{i=1}^{m-1} \theta_i(k) \phi_i, \quad (97)$$

where θ_i are the temporal coefficients of the eigenvectors ϕ_i . It comes directly, using Eq. (94), that

$$\begin{aligned} \mathbf{x}_{k+1} &= \mathcal{A} \mathbf{x}_k = \sum_{i=1}^{m-1} \theta_i(k) \mathcal{A} \phi_i = \sum_{i=1}^{m-1} \theta_i(k) \mu_i \phi_i \\ &= \mathcal{A}^k \mathbf{x}_1 = \sum_{i=1}^{m-1} \theta_i(1) \mu_i^k \phi_i, \end{aligned} \quad (98)$$

Using the work of Ref. 41, the matrix of the initial coefficient can be calculated using the relation

$$\boldsymbol{\theta}(1) = \boldsymbol{\phi}^+ \mathbf{x}_1. \quad (99)$$

VIII.B. Choice of the Parameters

Two main parameters are considered in the DMD framework initially introduced by Schmid.⁴ The first one is Δt , the constant time-step between two consecutive snapshots, while the second one is m , the total number of snapshots. Both of them require a good knowledge of the physical phenomenon under study. According to Schmid,⁴ the sample rate must be sufficiently high, about three times the Nyquist cutoff, to capture correctly the dynamics of an oscillatory flow. The idea is, then, to tune the sampling frequency based on the phenomenon the user wants to study. However, following Chen *et al.*,⁴² using a high sample rate, the snapshots are likely to be correlated in time. This is a problem since the method impose the use of a linear independent dataset to work properly. Finally, a high number, m , of snapshots could also affect the linear independency of the snapshots. In the algorithm used in the present work, a Gram-Schmidt step is included in the process to address this problem.^{10, 23}

IX. Case of a High Reynolds Number Supersonic Jet Flow

The present section is devoted to the study of a supersonic perfectly expanded jet flow. The geometry and flow configurations of interest are presented, followed by large eddy simulation results, which are compared to analytical, numerical and experimental data from the literature.^{43,44} The LES results provide a database for three DMD studies using the velocity magnitude, the vorticity, represented by the Q criterion, and the divergence of the flow velocity.

IX.A. Geometry and Mesh Configurations

Figure 2 illustrates a three-dimensional view of the representative domain for the jet flow simulations. The geometry resembles a frustrum of a cone with the jet entering the computational domain through the small base at $x = 0$, and leaving the domain at the large base at $x = 30D$. The radii of the entrance and exit plans are approximately $8D$ and $9D$, respectively. The authors have chosen not to include the nozzle geometry in the computational domain. Hence, the jet entrance is located at $x = 0$, for $|r|/D \leq 0.5$, where $|r| = \sqrt{y^2 + z^2}$ is the distance from the centerline in the radial direction and D is the incoming jet diameter. The computational domain is created in two steps. First, a 2-D region is generated. In the sequence, this region is rotated around the horizontal direction, x , indicated by the discontinuous blue line in Fig. 2, in order to generate a fully 3-D geometry. The rotation approach generates a singularity at the centerline of the domain. The treatment of this region is discussed in the boundary conditions section.

The commercial mesh generator ANSYS[®] ICEM CFD⁴⁵ is used for the creation of the 2-D domain for an azimuthal plane. The zones of this geometry are created based on results from simulations of previous work³¹ in order to refine the mesh in the shear layer region of the flow until $x = 10D$, after the end of the potential core. The mesh is, then, coarsened towards the outer regions of the domain in order to dissipate properties of the flow far from the jet. Such mesh refinement approach can avoid reflection of information into the domain. The radial and longitudinal dimensions of the smallest distance between mesh points of the computational grid are given by $(\Delta r)_{min} = 0.002$ and $(\Delta x)_{min} = 0.0126$, respectively. This minimal spacing occurs at the lipline of the jet and at the entrance of the computational domain. These dimensions are based on a reference grid of Mendez *et al.*^{43,46} The resulting computational grid is composed by 537 points in the axial direction, 442 points in the radial direction and 360 points in the azimuthal direction, yielding approximately 85 million grid points. For further details about the mesh generation, the reader is referred to the work of Junqueira-Junior.³²

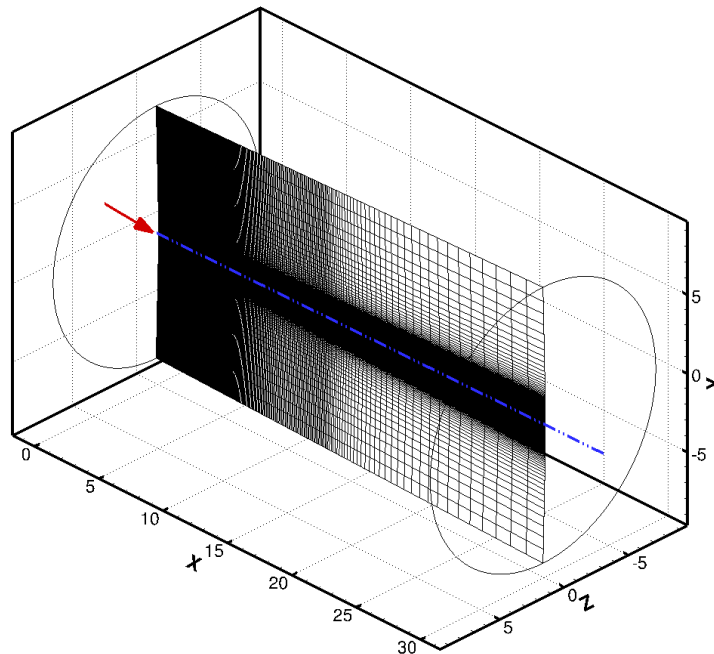


Figure 2. 3-D view of two XY slices of the grid, located above and below the centerline highlighted by a discontinuous blue line. The red arrow indicates the jet entrance inside the domain.

IX.B. Flow Configuration

The flow is characterized by an unheated perfectly expanded jet with a Mach number of 1.4 at the domain entrance. Therefore, the pressure ratio, $PR = P_j/P_\infty$, and the temperature ratio, $TR = T_j/T_\infty$, between the jet exit and the ambient freestream are equal to one, $PR = 1$ and $TR = 1$. The time step used in the simulation is constant and equal to 2.0×10^{-4} in dimensionless form. The Reynolds number of the jet is $Re = 1.57 \times 10^6$, based on the jet entrance diameter. This flow configuration is chosen due to the absence of strong shocks waves. Strong discontinuities must be carefully treated using numerical approaches, and the authors did not want to deal with those issues at the present time. Moreover, numerical and experimental data for a perfectly expanded jet flow configuration, such as the one used in the present work, are available in the literature such as the work of Mendez *et al.*^{43,46} and the work of Bridges and Wernet.⁴⁴

Properties of flow at the inlet and at the far field regions have to be provided to the code in order to impose the boundary conditions. Density, ρ , temperature, T , velocity, U , Reynolds number, Re , and specific heat at constant volume, C_v , are provided in the dimensionless form to the simulation. These dimensionless properties are given by

$$\begin{aligned} \rho_j &= 1.00 \quad , \quad \rho_\infty = 1.00 \quad , \\ T_j &= 1.00 \quad , \quad T_\infty = 1.00 \quad , \\ U_j &= 1.4 \quad , \quad U_\infty = 0.00 \quad , \\ Re_j &= 1.57 \times 10^6 \quad , \quad C_v = 1.786 \quad , \end{aligned} \tag{100}$$

where the j subscript stands for property at the jet entrance and the ∞ subscript stands for property at the far field region.

IX.C. Data Extraction Procedure

For the present study, data are extracted after a preliminary simulation is run in order to achieve a statistically steady state condition for the jet flow. This initial preliminary simulation lasts 96 dimensionless time units. For the current jet exit Mach number of $M_j = 1.4$, this simulation time represents approximately 3 flow-through times (FTT). One flow-through time is the time for a particle to cross the entire domain from the jet entrance to the domain exit. After the flow initialization process, the simulations are restarted and run for another period of time in which data of the flow are extracted and recorded at a fixed frequency.

Table 2. Data extraction characteristics

Simulation	$\Delta t c_\infty/D$	No. Extractions	Grid Size	Total Time	FTT
LES statistics	0.06	4096	500 × 425 (2-D)	245.76	≈ 8
DMD	0.12	256	473 × 412 × 180 (3-D)	30.72	≈ 1

The temporal characteristics of the data extraction are displayed in Tab. 2 for both the LES statistics and the DMD computations. These data processing methods are very different one from each other, especially because of the grid dimension. In the present work, the LES statistics are computed only along 2-D surfaces, whereas DMD calculations use three-dimensional snapshots as input. The snapshots extracted during the DMD process have more than 35 million points and they are stored in the PLOT3D format^a, adapted for structured meshes. The memory size of one snapshot, used for the DMD calculations, is about 1.5 Gb. On the other hand, the time-dependent LES surfaces are all included in one single CGNS file of 40 Gb. Finally, the total simulation time, necessary for obtaining the LES statistics, is higher than that used in Ref. 47 for the same purpose, and this can be considered as a fairly large time sample for an LES calculation. As indicated in Tab. 2, a total of 8 flow-through times have been used in order to obtain the LES statistics.

IX.D. Large Eddy Simulation Results

In this subsection, 2-D distributions of properties and profiles are collected from the compressible LES simulation and compared with numerical and experimental results from the literature.^{43,44,46} A longitudinal

^a<https://www.grc.nasa.gov/www/wind/valid/plot3d.html>

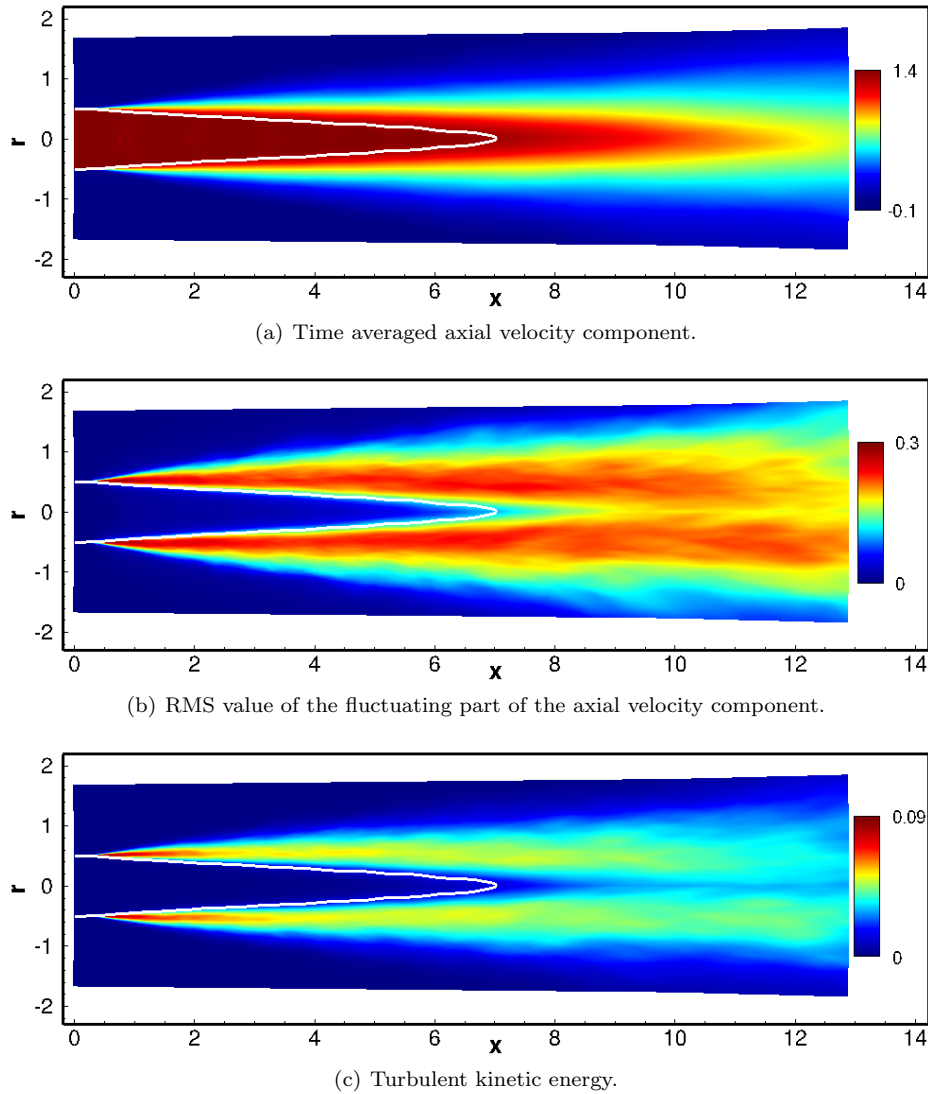


Figure 3. Contour plots of longitudinal planes of statistically converged jet properties. The white line defines the potential core of the jet, where $u = 0.95U_j$.

plane view of the statistically-converged time-averaged distributions of three flow properties, namely, axial velocity component, $\langle U \rangle$, RMS value of the fluctuating part of the axial velocity component, u_{rms} , and turbulent kinetic energy, k , are presented in Fig. 3. The statistical properties of the LES results are calculated using much more snapshots and with a more refined time increment than the numerical reference data.^{43,46} Each variable displays a fairly smooth flow field, confirming the good statistical convergence of the results. Moreover, the contours of $\langle U \rangle$, u_{rms} and k display a classical shape, with u_{rms} spreading along with the jet shear layer and with high values of k at the beginning of the mixing layer. The white solid line defines the jet potential core region, $U_j^{95\%}$, which is a characteristic parameter of jet flows. The potential core length, $\delta_j^{95\%}$, is defined as the distance from the jet entrance and along the centerline until the jet velocity reaches 95% of the velocity of the jet at the inlet.

In line with previous work, reported in Ref. 31, the current simulation aims to reduce the error with respect to the experimental data in Ref.⁴⁴ by refining the grid in the jet potential core. Table 3 presents the size of the potential cores for the current simulation, compared to the numerical results in Refs. 31, 43 and 46. The table presents the relative error compared to the experimental data.⁴⁴ The present LES calculations are performed on the same grid geometry used in Ref. 31, but with more points inside the potential core. As one can see in the table, the error has been reduced from 26% to 22%. The grid used in the present work needs to be further refined in order to overcome the dissipative characteristics of 2nd-order scheme used and,

hence, keep reducing the magnitude of error when compared to experimental data.

Table 3. Potential core length comparisons.

Simulation	$\delta_j^{95\%}$	Relative error
Current work	7.05	22%
Junqueira-Junior <i>et al.</i> ³¹	6.84	26%
Mendez <i>et al.</i> ^{43,46}	8.35	8%

The evolution of the averaged axial component of velocity and the evolution of the RMS value of the fluctuating part of the axial component of velocity along the centerline and the lipline are illustrated in Figs. 4 and 5, respectively. The solid line stands for the results of the present case, the open square symbols represent the LES results of Mendez *et al.*,^{43,46} while the triangular symbols stand for the experimental data of Bridges and Wernet.⁴⁴ The lipline is the surface defined over $r = 0.5D$, which represents the boundary of the jet at the entrance of the domain. The comparison of profiles indicates that distributions of $\langle U \rangle / U_j$ along the centerline correlates well with the references until $x = 7.0D$, where the grid has good resolution. The time averaged axial component of velocity start to correlate poorly with the reference when the mesh spacing increases, $x > 7.0D$, due to the mesh coarsening in the streamwise direction. The mesh coarsening is used in order to add artificial dissipation towards the exit of the domain, since the numerical framework does not have a sponge zone implemented. The time averaged axial component of velocity calculated along the lipline correlates well with the references until $x \approx 6.0D$. The magnitude of $\langle U \rangle / U_j$ along the lipline is underestimated for $x > 6.0D$.

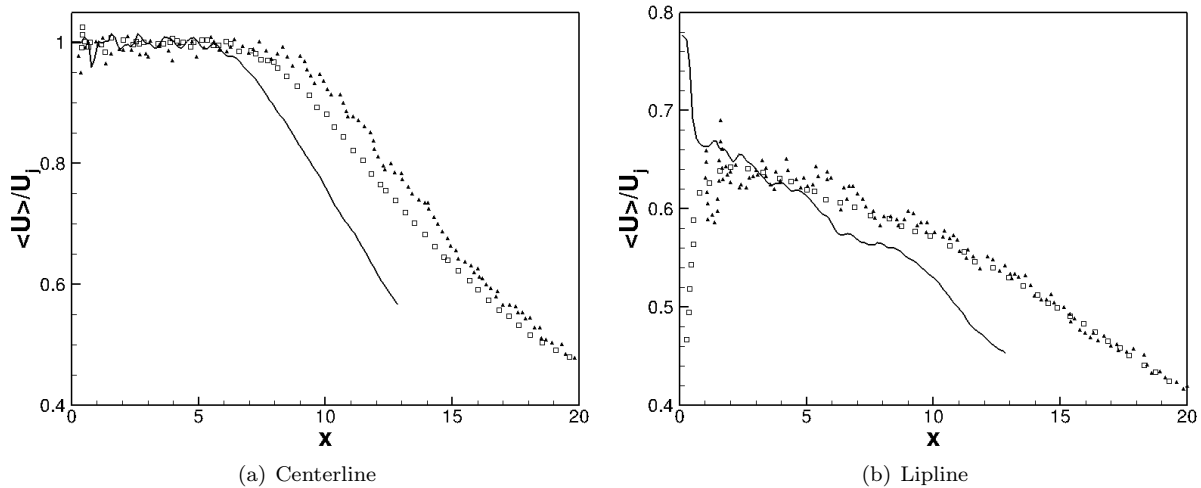


Figure 4. Averaged axial component of velocity along the centerline and lipline. The solid line stands for the results of the present case, the open square symbols represent the numerical references^{43,46} and the triangular symbols are the experimental data.⁴⁴

The distribution of u_{rms}/U_j calculated along the centerline fits the numerical and experimental reference distributions of the same property for $x < 4.0D$. However, it presents an overestimated distribution of u_{rms}/U_j when compared with both numerical and experimental data at other positions along the centerline. The numerical reference has also calculated an overestimated distribution of u_{rms}/U_j along the centerline when compared to the experimental reference at $x > 5.0D$. The distribution of u_{rms}/U_j along the lipline calculated by the current work and by the numerical reference present similar behavior. Nonetheless, the distributions are overestimated when compared to the experimental data.

IX.E. Dynamic Mode Decomposition Results

The streaming version²³ of the *total-least-squares* DMD algorithm²⁴ on volumetric data extracted during the large eddy simulations described in Sect. IX is computed in the present work. Considering that the DMD calculation is performed in serial mode, the computer memory is the limiting factor to compute the DMD

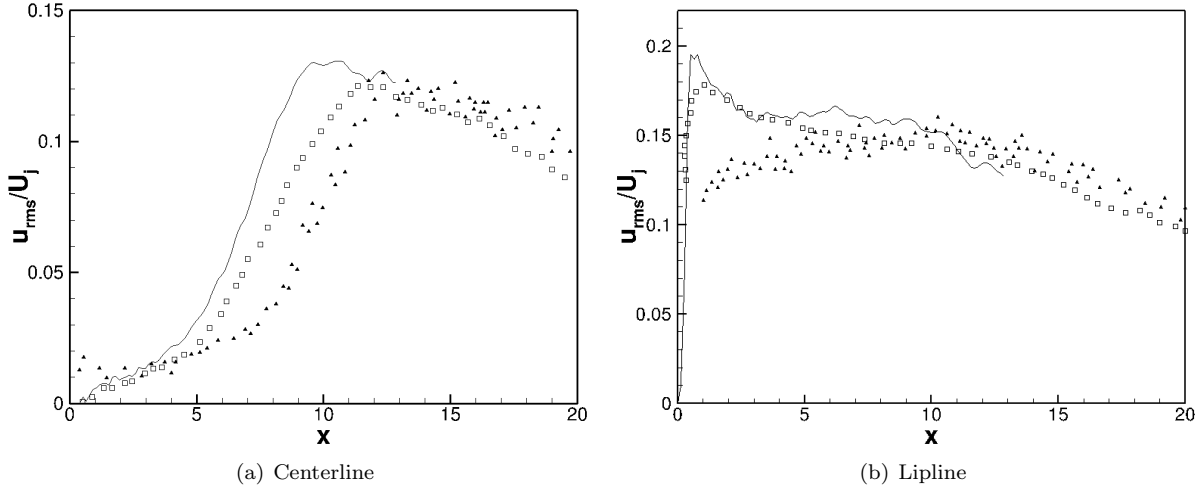


Figure 5. RMS value of the fluctuating part of the axial component of velocity along the centerline and lipline. The solid line stands for the results of the present case, the open square symbols represent the numerical references^{43,46} and the triangular symbols are the experimental data.⁴⁴

modes. The DMD calculation is run on a single processor with 128 GB of RAM. According to Hemati *et al.*,²³ the computational cost of the algorithm to calculate the DMD eigen-elements is $\mathcal{O}(nr^2)$, where n and r are the snapshot dimension and the maximum rank of the DMD operator, respectively. For the latter parameter, the streaming version of the DMD algorithm includes a compression step allowing to set it arbitrarily. Then, the choice of these parameters is a compromise between spatial and spectral resolution. The jet entrance, the potential core and the near field of the jet are included in the computational domain in order to prioritize the spatial aspects of the flow.

Therefore, the results should include the aerodynamic structures as well as the generated acoustic waves. However, the original snapshots have been under-sampled in spatial resolution in order to handle manageable snapshots. The dimensions of the snapshots are specified in Tab. 2, counting approximately 35 million grid points. Finally, considering 256 snapshots without subtracting the mean, r has been set equal to 50, which was the higher affordable number of retained modes in relation to the available computer memory. In the present case, three variables were extracted from the LES calculations. Hence, three different DMD reconstruction procedures were performed, using snapshots of the velocity magnitude, the vorticity, based on the Q criterion, and the divergence of the velocity. In the following subsections, results are discussed regarding their spectral content (Sect. IX.E.1) and spatial shape (Sect. IX.E.2).

IX.E.1. Spectral Analysis

Figure 6 displays three different ways of representing the DMD spectrum obtained after the DMD computation using snapshots of the velocity magnitude. Figure 6(a) presents the 50 eigenvalues of \mathcal{A} DMD linear operator. The symbols are colored by the initial amplitude of the DMD modes, $\|\theta_i(1)\|$, which are defined in Eq. (99). The choice of this parameter to differentiate the dynamic modes comes from Eqs. (93) and (98). The initial amplitude of the DMD modes has also been taken into account by Sayadi *et al.*⁷ All dynamic modes which are located inside the unit circle are stable. The only one DMD mode located on the unit circle is a steady mode which, in general, retrieves the mean characteristics of the flow.⁴² The stable dynamic modes are unsteady and have a complex conjugate, symmetric with respect to the $\text{Im}(\mu_i) = 0$ axis. In Fig. 6 (b), the growth rate of each mode, σ_i , is plotted versus the frequency, ω_i . A mode is stable if σ_i is negative, which is in agreement with the discussion considering Fig. 6(a). Finally, Fig. 6 (c) presents the most amplified DMD mode as a function of the Strouhal number. Four dynamic modes displaying a high amplitude have been selected. In Figs. 6(b) and (c), it appears that the stability of the mode is not linked with its initial amplitude. The DMD Mode 5 is more stable than the DMD Mode 7 ($\sigma_5 < \sigma_7$). However, $\|\theta_5(1)\|$ is larger than $\|\theta_7(1)\|$. Therefore, one can state that the dynamic mode 5 is initially more amplified than the dynamic mode 7, but it decays more quickly as the simulation advances in time.

Figures 7 and 8 show two different sets of spectra obtained from the DMD computations using snapshots

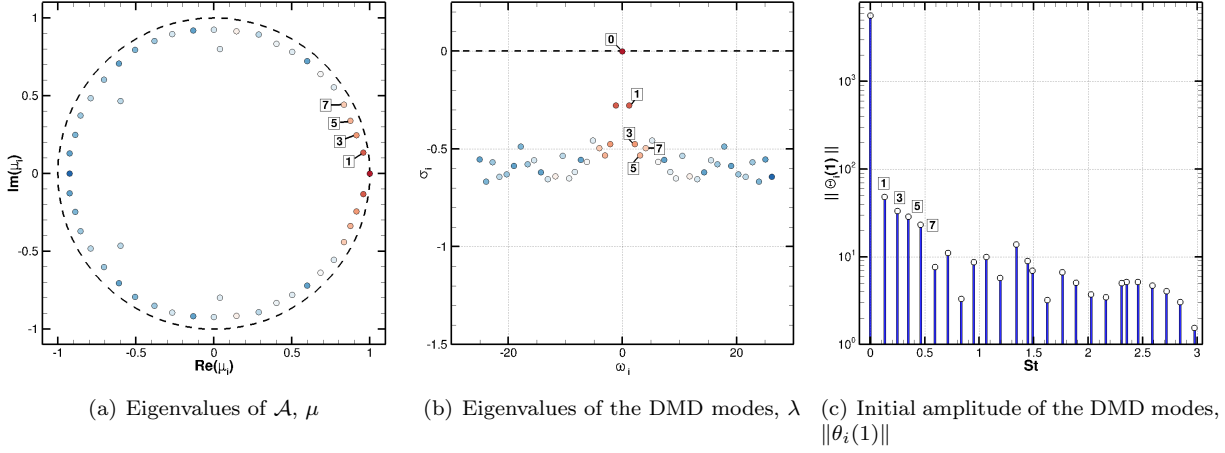


Figure 6. Spectra from DMD computation using snapshots of velocity magnitude. In (a) and (b), the symbols are colored by the mode amplitude, $\|\theta_i(1)\|$.

of the vorticity, based on the Q-criterion, and the divergence of the velocity, respectively. Once again, all dynamic modes are stable, but the one representing the mean flow is neutrally stable. More DMD modes have been highlighted by a number in order to identify them in each spectrum.

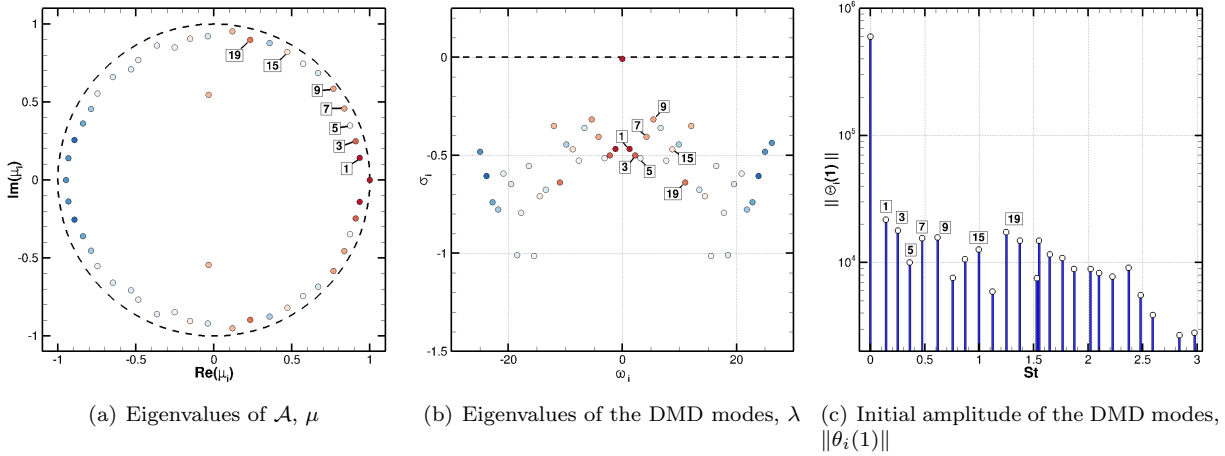


Figure 7. Spectra from DMD computation using snapshots of vorticity. In (a) and (b), the symbols are colored by the mode amplitude, $\|\theta_i(1)\|$.

One can observe in Figs. 6(c), 7(c) and 8(c) that every spectra contain a dynamic mode at $St \approx 0.25$ and at $St \approx 0.48$. The clustering around specific frequencies for different DMD analyses denotes important dynamic activity at these frequencies. The DMD modes associated to each frequency are shown in Tab. 4. These characteristic frequencies coincide with the experimental far field pressure peaks observed by Bridges *et al.*⁴⁴ In the next subsection, the spatial shapes of these dynamic modes, given in Tab. 4, are discussed in more detail.

Table 4. Characteristic frequencies and associated DMD modes

St	Velocity magnitude	Vorticity	Divergence of velocity
0.25	3	3	7
0.48	7	7	5

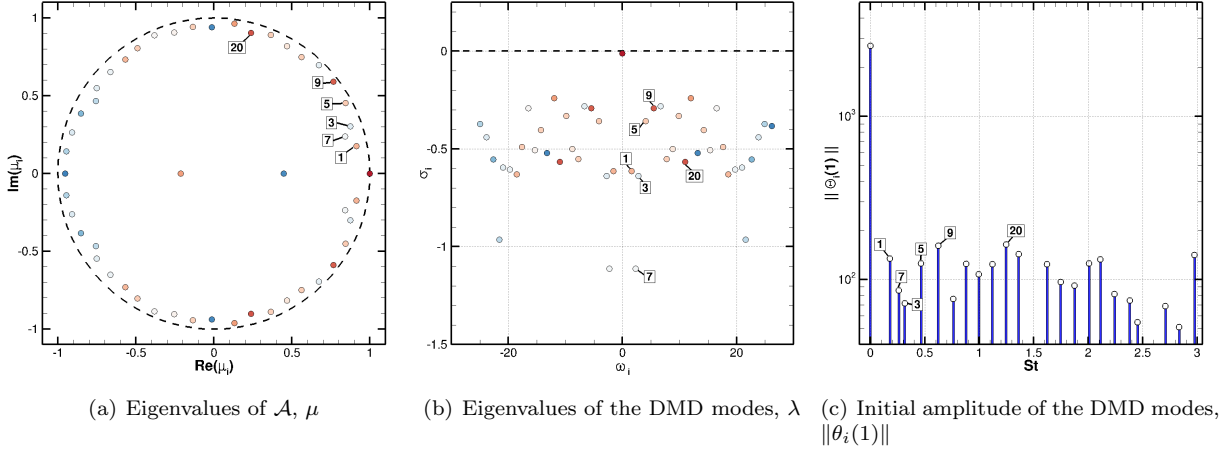


Figure 8. Spectra from DMD computation using snapshots of divergence of velocity. In (a) and (b), the symbols are colored by the mode amplitude, $\|\theta_i(1)\|$.

IX.E.2. Spatial Modes Analysis

The averaged axial velocity component of the steady DMD mode is shown in Fig. 9, using the same color coding for the contours as the LES mean flow illustrated in Fig. 3. One can notice a white gap around the centerline of the flow. The gap is created because the radial coordinate of the snapshot grid starts at the 20th point in the radial direction, in order to reduce the computational cost of the DMD computation. The DMD mode has been reconstructed by multiplying the mode shape by its initial amplitude $\|\theta_0(1)\|$. A fairly good agreement between the DMD calculation and the large eddy simulation is found regarding the potential core length as well as the contour levels, even considering that the sample rate and the number of snapshots are quite different in the DMD calculation when compared to the LES statistics calculation.

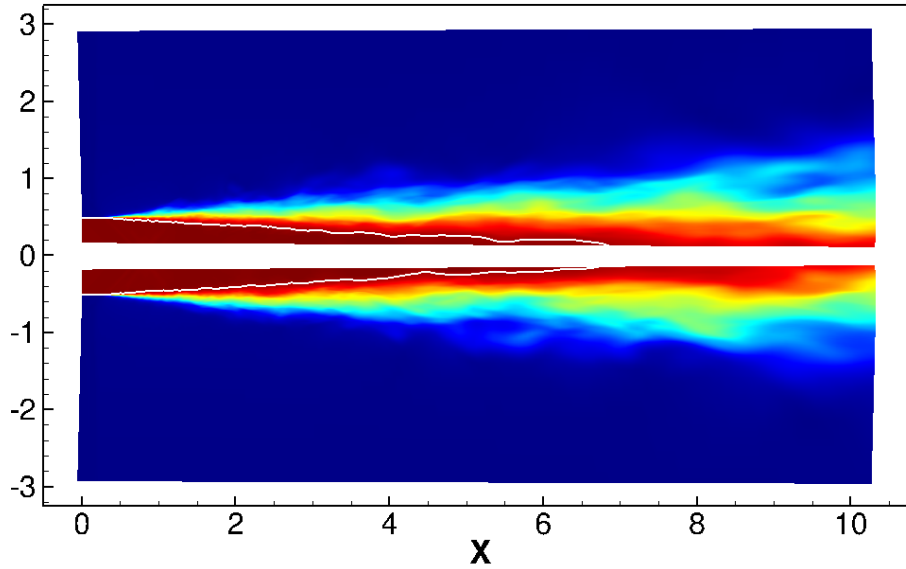


Figure 9. Slice of the three dimensional steady DMD mode for the velocity magnitude. The white line defines the potential core limits. Contours are the same as in Fig. 3.

As mentioned in the previous subsection, the experimental far field pressure spectrum of Bridges *et al.*⁴⁴ displays two peaks at $St \approx 0.25$ and $St \approx 0.48$. Modes at the same frequencies are observable in the three DMD analyses performed in the present study. Figure 10 displays the DMD modes associated to the first frequency, $St \approx 0.25$, while Fig. 11 shows the DMD modes associated to $St \approx 0.48$. In both figures, isosurfaces and 2-D cut planes of velocity magnitude, vorticity (Q criterion) and divergence of velocity

are presented. Considering the high Reynolds number of the present work, and the rapid transition from laminar flow at the jet inlet to a turbulent jet mixing layer, it is possible to observe coherent behavior in the jet dynamics. Moreover, the three variables, for which the DMD computations were performed, bring different information about the flow dynamics. While the vorticity modes seem to enlighten the mixing layer dynamics, the velocity magnitude as well as the divergence of velocity seem to highlight the aeracoustic dynamics.

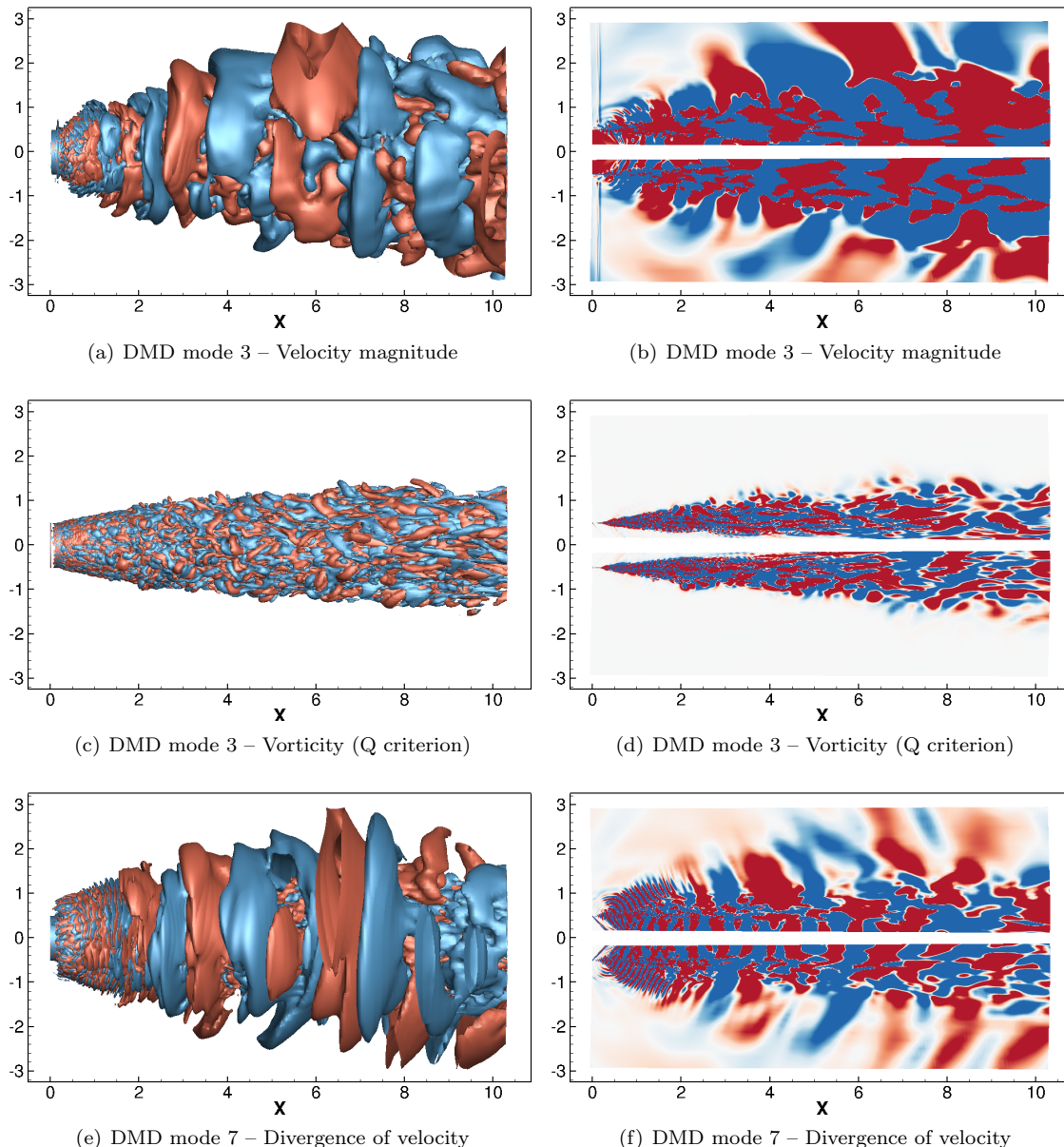


Figure 10. Visualization of the DMD modes found at $St \approx 0.25$. (a) and (b) display the real part of Mode 3 extracted from the DMD analysis using snapshots of velocity magnitude, (c) and (d) display the real part of Mode 3 extracted from the DMD analysis using snapshots of vorticity (Q criterion), and (e) and (f) display the real part of Mode 7 extracted from the DMD analysis using snapshots of divergence of velocity. The left and right columns show 3-D isosurfaces and 2-D cut-plane visualizations of the modes, respectively (positive in red and negative in blue).

Figures 10 and 11 indicate that, until $x \approx 1$, small coherent vortical structures are growing in the jet mixing layer, generating small acoustic waves. Further downstream, the flow has already transitioned and large acoustic waves are generated and are propagated in the downstream direction. As expected, the wavelength of the large acoustic waves depends on the DMD mode frequency. One can see, when comparing, for instance, Fig. 10(a) with Fig. 11(a), or Fig. 10(e) with Fig. 11(e), that the wavelength of the coherent

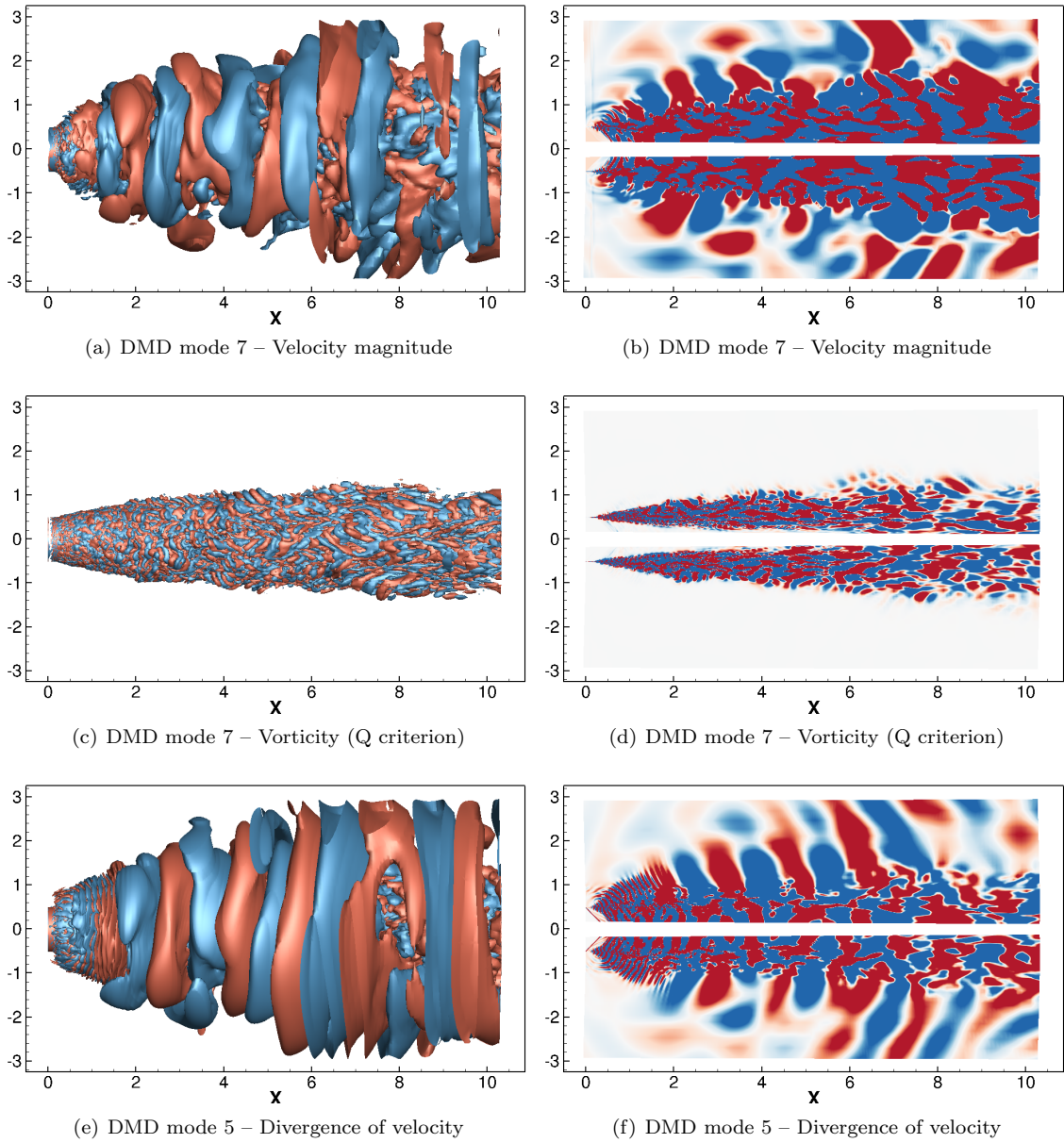


Figure 11. Visualization of the DMD modes found at $St \approx 0.48$. (a) and (b) display the real part of Mode 7 extracted from the DMD analysis using snapshots of velocity magnitude, (c) and (d) display the real part of Mode 7 extracted from the DMD analysis using snapshots of vorticity (Q criterion), and (e) and (f) display the real part of Mode 5 extracted from the DMD analysis using snapshots of divergence of velocity. The left and right columns show 3-D isosurfaces and 2-D cut-plane visualizations of the modes, respectively (positive in red and negative in blue).

structures is divided by two when the frequency is doubled. Moreover, it is easy to verify, for instance, in Fig. 11(f), the relation between the wavelength of the large acoustic waves and the actual frequency of the DMD mode, ω_i .

Another interesting aspect is the presence of small vortices in the inner mixing layer, at the interface with the potential core. These structures are visible in Figs. 10(d) and 11(d). Unfortunately, due to the absence of grid points along the centerline itself in the grid used to extract the data for in the present DMD calculations, the influence of these small vortices at the end of the potential core is not accessible in the present case. Future work should consider a snapshot grid covering all the inner part of the jet. Finally, one can see in Fig. 11(c) that the vortex filaments in the mixing layer seem to suffer a three-dimensional helicoidal distortion around the jet mixing layer. The work of Violato and Scarano,⁴⁸ who performed experiments for a low Reynolds free water jet, using time-resolved tomographic particle image velocimetry (TR-TOMO PIV),

can certainly help in the understanding of this type of fundamental aspect in the current jet dynamics.

X. Concluding Remarks

The present work is concerned with the study of the aerodynamics of a perfectly expanded supersonic jet flow. It is expected that the flow data and the reduced order model here generated could be used in the future for performing aeroacoustic studies of jet flows. An implicit large eddy simulation (LES) formulation for compressible flows, based on the System I set of equations, is used. A streaming version of the total-least-squares DMD algorithm is chosen to run concurrently with the LES simulation and provide an additional form of studying the more relevant aspects of the jet dynamics.

LES of a high Reynolds perfectly expanded supersonic jet flow configuration is performed on a computational mesh with 85 million grid points. Statistical data are extracted from the simulations and present good agreement with the numerical and experimental reference work, at least near the jet inlet region where the mesh is well refined. However, this is not the case when the jet moves away from the domain entrance. As a result, the potential core length calculated by the present LES is underestimated. Such behavior could be expected since the low order numerical scheme of the numerical solver presently used would probably require quite extensive mesh refinements. The work also presents three DMD analyses, which have been performed by extracting large three-dimensional snapshots from the LES results. These DMD computations concerned the velocity magnitude, the vorticity, based on the Q criterion, and the divergence of the velocity. Two frequencies are identified for which all DMD calculations identify a dynamic mode with relevant flow structures. These frequencies agree with those of relevant dynamics identified in previous experimental work available in the literature. The analysis of all the dynamic modes brought new insights on the jet dynamics regarding the vortical structures and the acoustic wave patterns.

At the time of this writing, the LES solver is being adapted in order to include parallel I/O features. This capability will open new opportunities in term of additional grid resolution that would allow a reduction in the difference between the results calculated by the authors and other data, computational or experimental, available in the literature. Moreover, the DMD algorithm here implemented should also be parallelized in order to allow handling larger snapshots and, hence, the extraction of more information from the flow, especially at the centerline of the jet and further downstream of the jet entrance. Hopefully, these modifications will allow sufficient mesh refinement, both for the LES calculations and for DMD analyses, that the present tool will be useful for studies of the jet aeroacoustics.

Acknowledgments

The authors gratefully acknowledge the partial support for this research provided by Conselho Nacional de Desenvolvimento Científico e Tecnológico, CNPq, under the Research Grants No. 309985/2013-7, No. 400844/2014-1, No. 443839/2014-0 and No. 150450/2016-8. The authors are also indebted to the partial financial support received from Fundação de Amparo à Pesquisa do Estado de São Paulo, FAPESP, under the Research Grants No. 2013/07375-0 and No. 2013/21535-0.

References

- ¹Lumley, J. L., *Stochastic Tools in Turbulence*, Academic Press, New York, 1970.
- ²Sirovich, L., “Turbulence and the Dynamics of Coherent Structures. Part I: Coherent Structures,” *Quarterly of Applied Mathematics*, Vol. 45, No. 3, 1987, pp. 561–571.
- ³Berkooz, G., Holmes, P., and Lumley, J. L., “The Proper Orthogonal Decomposition in the Analysis of Turbulent Flows,” *Annual Review of Fluid Mechanics*, Vol. 25, No. 1, 1993, pp. 539–575.
- ⁴Schmid, P. J., “Dynamic Mode Decomposition of Numerical and Experimental Data,” *Journal of Fluid Mechanics*, Vol. 656, 2010, pp. 5–28.
- ⁵Seena, A. and Sung, H. J., “Dynamic Mode Decomposition of Turbulent Cavity Flows for Self-Sustained Oscillations,” *International Journal of Heat and Fluid Flow*, Vol. 32, No. 6, 2011, pp. 1098–1110.
- ⁶Grilli, M., Schmid, P. J., Hickel, S., and Adams, N. A., “Analysis of Unsteady Behaviour in Shockwave Turbulent Boundary Layer Interaction,” *Journal of Fluid Mechanics*, Vol. 700, 2012, pp. 16–28.
- ⁷Sayadi, T., Schmid, P., Nichols, J. W., and Moin, P., “Dynamic Mode Decomposition of Controlled H- and K-Type Transitions,” Tech. rep., Annual Research Briefs, 2013.
- ⁸Tang, Z. and Jiang, N., “Dynamic Mode Decomposition of Hairpin Vortices Generated by a Hemisphere Protuberance,” *Science China Physics, Mechanics and Astronomy*, Vol. 55, No. 1, 2012, pp. 118–124.

- ⁹Bagheri, S., “Koopman-Mode Decomposition of the Cylinder Wake,” *Journal of Fluid Mechanics*, Vol. 726, 2013, pp. 596–623.
- ¹⁰Tissot, G., Cordier, L., Benard, N., and Noack, B. R., “Dynamic Mode Decomposition of PIV Measurements for Cylinder Wake Flow in Turbulent Regime,” *Proceedings of Turbulence and Shear Flow Phenomena Conferences, Eight International Symposium on Turbulence and Shear Flow Phenomena*, Begel House Inc., 2013.
- ¹¹Jourdain, G., Eriksson, L.-E., Kim, S. H., and Sohn, C. H., “Application of Dynamic Mode Decomposition to Acoustic-Modes Identification and Damping in a 3-Dimensional Chamber with Baffled Injectors,” *Journal of Sound and Vibration*, Vol. 332, No. 18, 2013, pp. 4308–4323.
- ¹²Abou-Taouk, A., Sadasivuni, S., Lörstad, D., Ghenadie, B., and Eriksson, L.-E., “CFD Analysis and Application of Dynamic Mode Decomposition for Resonant-Mode Identification and Damping in an SGT-100 DLE Combustion System,” *Proceedings of the 7th European Combustion Meeting*, 2015.
- ¹³Lárusson, R., Hafsteinnsson, H. E., Andersson, N., and Eriksson, L.-E., “Investigation of Supersonic Jet Flow Using Modal Decomposition,” *20th AIAA/CEAS Aeroacoustics Conference*, 2014.
- ¹⁴Schmid, P. J., “Application of the Dynamic Mode Decomposition to Experimental Data,” *Experiments in Fluids*, Vol. 50, No. 4, 2011, pp. 1123–1130.
- ¹⁵Schmid, P. J., Li, L., Juniper, M., and Pust, O., “Applications of the Dynamic Mode Decomposition,” *Theoretical and Computational Fluid Dynamics*, Vol. 25, No. 1-4, 2011, pp. 249–259.
- ¹⁶Schmid, P. J., Violato, D., and Scarano, F., “Decomposition of Time-Resolved Tomographic PIV,” *Experiments in Fluids*, Vol. 52, No. 6, 2012, pp. 1567–1579.
- ¹⁷Stegeman, P., Soria, J., and Ooi, A., “Dynamic Mode Decomposition of Near Nozzle Instabilities in Large-Eddy Simulations of Under-Expanded Circular Jets.” *Australasian Fluid Mechanics Conference*, RMIT University, 08–11 December 2014, pp. 1–4.
- ¹⁸Wan, Z.-H., Zhou, L., Wang, B.-F., and Sun, D.-J., “Dynamic Mode Decomposition of Forced Spatially Developed Transitional Jets,” *European Journal of Mechanics-B/Fluids*, Vol. 51, 2015, pp. 16–26.
- ¹⁹Wynn, A., Pearson, D., Ganapathisubramani, B., and Goulart, P., “Optimal Mode Decomposition for Unsteady Flows,” *Journal of Fluid Mechanics*, Vol. 733, 2013, pp. 473–503.
- ²⁰Jovanović, M. R., Schmid, P. J., and Nichols, J. W., “Sparsity-Promoting Dynamic Mode Decomposition,” *Physics of Fluids*, Vol. 26, No. 2, 2014, pp. 024103.
- ²¹Williams, M. O., Kevrekidis, I. G., and Rowley, C. W., “A Data-Driven Approximation of the Koopman Operator: Extending Dynamic Mode Decomposition,” *Journal of Nonlinear Science*, Vol. 25, No. 6, 2015, pp. 1307–1346.
- ²²Williams, M., Rowley, C. W., and Kevrekidis, I. G., “A Kernel-Based Approach to Data-Driven Koopman Spectral Analysis,” *AIMS Journals*, arxiv.org/pdf/1411.2260v4.pdf, 2015.
- ²³Hemati, M. S., Williams, M. O., and Rowley, C. W., “Dynamic Mode Decomposition for Large and Streaming Datasets,” *Physics of Fluids*, Vol. 26, No. 11, 2014, pp. 111701.
- ²⁴Hemati, M. S. and Rowley, C. W., “De-Biasing the Dynamic Mode Decomposition for Applied Koopman Spectral Analysis,” arxiv.org/pdf/1502.03854v2.pdf, 2015.
- ²⁵Vreman, A. W., *Direct and Large-Eddy Simulation of the Compressible Turbulent Mixing Layer*, Ph.D. thesis, Universiteit Twente, 1995.
- ²⁶Vremant, B., Geurts, B., and Kuerten, H., “A Priori Tests of Large Eddy Simulation of the Compressible Plane Mixing Layer,” *Journal of Engineering Mathematics*, Vol. 29, 1995, pp. 299–327.
- ²⁷Garnier, E., Adams, N., and Sagaut, P., *Large Eddy Simulation for Compressible Flows*, Springer, 2009.
- ²⁸Sagaut, P., *Large Eddy Simulation for Incompressible Flows*, Springer, 2002.
- ²⁹Eidson, T. M., “Numerical Simulation of the Turbulent Rayleigh–Bénard Problem Using Subgrid Modelling,” *Journal of Fluid Mechanics*, Vol. 158, 1985, pp. 245–268.
- ³⁰Junqueira-Junior, C., Yamouni, S., Azevedo, J. L. F., and Wolf, W. R., “Large Eddy Simulations of Supersonic Jet Flows for Aeroacoustic Applications,” AIAA Paper No. 2015-3306, *Proceedings of the 33rd AIAA Applied Aerodynamics Conference*, Dallas, TX, June 2015.
- ³¹Junqueira-Junior, C., Yamouni, S., Azevedo, J. L. F., and Wolf, W. R., “Influence of Different Subgrid Scale Models in LES of Supersonic Jet Flows,” AIAA Paper No. 2016-4093, *Proceedings of the 46th AIAA Fluid Dynamics Conference*, Washington, DC, June 2016.
- ³²Junqueira-Junior, C., *Development of a Parallel Solver for Large Eddy Simulation of Supersonic Jet Flows*, Ph.D. thesis, Instituto Tecnológico de Aeronáutica, São José dos Campos, SP, Brasil, 2016.
- ³³Bigarella, E. D. V., *Three-Dimensional Turbulent Flow Over Aerospace Configurations*, M.Sc. Thesis, Instituto Tecnológico de Aeronáutica, São José dos Campos, SP, Brasil, 2002.
- ³⁴Turkel, E. and Vatsa, V. N., “Effect of Artificial Viscosity on Three-Dimensional Flow Solutions,” *AIAA Journal*, Vol. 32, No. 1, 1994, pp. 39–45.
- ³⁵Jameson, A. and Mavriplis, D., “Finite Volume Solution of the Two-Dimensional Euler Equations on a Regular Triangular Mesh,” *AIAA Journal*, Vol. 24, No. 4, Apr. 1986, pp. 611–618.
- ³⁶Jameson, A., Schmidt, W., and Turkel, E., “Numerical Solutions of the Euler Equations by Finite Volume Methods Using Runge-Kutta Time-Stepping Schemes,” AIAA Paper 81-1259, *Proceedings of the AIAA 14th Fluid and Plasma Dynamic Conference*, Palo Alto, California, USA, June 1981.
- ³⁷Long, L. N., Khan, M., and Sharp, H. T., “A Massively Parallel Three-Dimensional Euler/Navier-Stokes Method,” *AIAA Journal*, Vol. 29, No. 5, 1991, pp. 657–666.
- ³⁸Tu, J. H., Rowley, C. W., Kutz, J. N., and Shang, J. K., “Spectral Analysis of Fluid Flows Using Sub-Nyquist-Rate PIV Data,” *Experiments in Fluids*, Vol. 55, No. 9, 2014, pp. 1–13.
- ³⁹Rowley, C. W., Mezić, I., Bagheri, S., Schlatter, P., and Henningson, D. S., “Spectral Analysis of Nonlinear Flows,” *Journal of Fluid Mechanics*, Vol. 641, 2009, pp. 115–127.

⁴⁰Hemati, M. S., Deem, E. A., Williams, M. O., Rowley, C. W., and Cattafesta, L. N., “Improving Separation Control with Noise-Robust Variants of Dynamic Mode Decomposition,” *54th AIAA Aerospace Sciences Meeting*, 2016.

⁴¹Kutz, J. N., Fu, X., and Brunton, S. L., “Multiresolution Dynamic Mode Decomposition,” *SIAM Journal on Applied Dynamical Systems*, Vol. 15, No. 2, 2016, pp. 713–735.

⁴²Chen, K. K., Tu, J. H., and Rowley, C. W., “Variants of Dynamic Mode Decomposition: Boundary Condition, Koopman, and Fourier Analyses,” *Journal of Nonlinear Science*, Vol. 22, No. 6, 2012, pp. 887–915.

⁴³Mendez, S., Shoeybi, M., Sharma, A., Ham, F. E., Lele, S. K., and Moin, P., “Large-Eddy Simulations of Perfectly-Expanded Supersonic Jets: Quality Assessment and Validation,” AIAA Paper No. 2010-0271, *Proceedings of the 48th AIAA Aerospace Sciences Meeting Including The New Horizons Forum and Aerospace Exposition*, Orlando, FL, January 2010.

⁴⁴Bridges, J. and Wernet, M. P., “Turbulence Associated with Broadband Shock Noise in Hot Jets,” AIAA Paper No. 2008-2834, *Proceedings of the 14th AIAA/CEAS Aeroacoustics Conference and 29th AIAA Aeroacoustics Conference*, Vancouver, BC, Canada, May 2008.

⁴⁵ANSYS, “<http://www.ansys.com/>,” .

⁴⁶Mendez, S., Shoeybi, M., Sharma, A., Ham, F. E., Lele, S. K., and Moin, P., “Large-Eddy Simulations of Perfectly-Expanded Supersonic Jets Using an Unstructured Solver,” *AIAA Journal*, Vol. 50, No. 5, May 2012, pp. 1103–1118.

⁴⁷Bres, G. A., Nichols, J. W., Lele, S. K., and Ham, F. E., “Towards Best Practices for Jet Noise Predictions with Unstructured Large Eddy Simulations,” AIAA Paper No. 2012-2965, *Proceedings of the 42nd AIAA Fluid Dynamics Conference and Exhibit*, New Orleans, Louisiana, June 2012.

⁴⁸Violato, D. and Scarano, F., “Three-Dimensional Vortex Analysis and Aeroacoustic Source Characterization of Jet Core Breakdown,” *Physics of Fluids*, Vol. 25, No. 1, 2013, pp. 015112.